Kovove Mater. 63 2025 331–356
DOI: 10.31577/km.2025.5-6.331

Influence of heat treatments and hot isostatic processes (HIP) on microstructure and mechanical behavior of Ti-6Al-4V alloy produced by Powder Bed Fusion Using Electron Beam (PBF-EB)

Mutlu Karasoglu[1]*, Evren Yasa[2], Evren Tan[3], Sina Kavak[3], Emrecan Soylemez[4], Melih Cemal Kuşhan[5]

[1] *Eskişehir Technical University, Department of Mechanical Engineering, Eskişehir 26555, Turkey*
[2] *University of Sheffield, Advanced Manufacturing Research Centre, Sheffield S60 5TZ, United Kingdom*
[3] *Mechanical Design Technologies Department, ASELSAN Inc, EKIM Laboratory, Ankara 06200, Turkey*
[4] *Department of Mechanical Engineering, Istanbul Technical University, Istanbul 34437, Turkey*
[5] *Eskişehir Osmangazi University, Department of Aeronautical Engineering, Eskişehir 26040, Turkey*

Received 02 November 2025, received in revised form 12 December 2025, accepted 15 December 2025

Abstract

This study investigates the effects of heat treatments and hot isostatic pressing (HIP) on the microstructure and mechanical behavior of Ti-6Al-4V parts manufactured by electron-beam powder bed fusion. Solution treatment at 950 °C, followed by aging at 500–600 °C, did not alter porosity. Aging increased the α-phase ratio and compensated for the strength reduction induced by ST. All HIP cycles significantly reduced pore size and pore count, with the 800 °C/200 MPa cycle yielding the highest average relative density of 99.86 %, resulting in a maximum yield strength of 948 MPa and a maximum ultimate tensile strength of 1013 MPa. An 800 °C/200 MPa HIP cycle increased ductility while maintaining strength, owing to limited α-lath coarsening. Super-transus HIP at 1050 °C/100 MPa transformed columnar β grains into equiaxed structures, causing significant α-lath coarsening, a loss of mechanical strength, and increased anisotropy. These findings emphasize the need to optimize post-processing to balance porosity elimination, microstructural refinement, and mechanical performance in Ti-6Al-4V components.

K e y w o r d s: additive manufacturing, Powder Bed Fusion Using Electron Beam (PBF-EB), Ti-6Al-4V, heat treatment, hot isostatic pressing

1. Introduction

Additive manufacturing (AM) is a rapidly growing process that offers major advantages over conventional manufacturing methods. Its layer-by-layer approach enables the fabrication of fully dense, geometrically complex metal parts while reducing material waste and costs, which are especially important in aerospace applications [1].

Powder Bed Fusion Using Electron Beam (PBF-EB) is a powder bed fusion additive manufacturing method that uses a high-energy electron beam to selectively melt each powder layer. The electron beam possesses high power and can be manipulated at exceptional speeds, enabling high operating temperatures and the implementation of innovative melting strategies. Additionally, due to its high-temperature processing, PBF-EB yields lower residual stresses than other methods, such as Laser Powder Bed Fusion (LPBF) [2]. PBF-EB is performed under vacuum and can produce high-density parts from various engineering alloys [3].

Ti-6Al-4V is the most widely used titanium alloy in aerospace applications, including jet engines, gas turbines, and airframe components. Its prevalence is due to a unique combination of high strength, low density, excellent fracture toughness, and superior corrosion resistance [4]. Furthermore, due to its excellent corrosion resistance and biocompatibility, the Ti-6Al-4V alloy is widely used in biomedical implants [5]. On the

*Corresponding author: e-mail address: mutlukarasoglu@eskisehir.edu.tr

other hand, machining Ti-6Al-4V is challenging due to its low thermal conductivity, low specific heat capacity, and tendency to soften thermally at high temperatures. As a result, significant efforts have been made to advance additive manufacturing processes for titanium alloys [6].

Ti-6Al-4V is a biphasic alloy that contains a mixture of α and β phases in its microstructure. This phase mixture arises because the transformation of the β phase at room temperature is inhibited by β-stabilizing elements, such as vanadium [7]. The microstructure of as-built Ti-6Al-4V parts produced by PBF-EB differs from that of conventional cast and wrought Ti-6Al-4V alloys due to the high cooling rates and directional solidification characteristic of the PBF-EB process. As-built microstructure contains columnar prior β grains aligned parallel to the build direction, with a lamellar $\alpha + \beta$ structure (Widmanstätten morphology) within these prior β grains. A grain boundary α phase is also observed along the borders of the prior β grains [8]. The microstructure of the Ti-6Al-4V alloy is determined by the thermal history of the PBF-EB process, as detailed in [9]. In the first stage of the process, the melt pool solidifies into the β phase, cools rapidly to chamber temperature, and undergoes a transformation from the β phase to the martensitic α' phase. In the second stage, the martensitic α' phase is exposed to relatively high chamber temperatures (650–750 °C) until the build is complete, resulting in decomposition of the α' phase into an $\alpha + \beta$ structure. In the third stage, the build chamber slowly cools to room temperature.

Post-processing operations, such as heat treatments (HT) and hot isostatic pressing (HIP), are applied to PBF-EB parts to modify their microstructure and mechanical properties. Cunningham et al. investigated the effect of HIP at 900 °C for 2 hours under 103 MPa in an argon environment and concluded that HIP is a highly effective process, significantly reducing both the number and size of the pores [10]. They used two different types of powders, produced by plasma atomization and plasma rotating electrode processes. They demonstrated that HIP eliminated lack-of-fusion defects in parts produced from both powders at their equipment scale. Furthermore, HIP reduced the number of gas porosities per mm^2 from 263 to 35 and decreased the average equivalent diameter from 10 to 3 μm in parts made from plasma-atomized powders. Similarly, for parts made from plasma rotating electrode powders, the number of gas porosities per mm^2 decreased from 7 to 1, and the average equivalent diameter reduced from 7 to 5 μm. In another study, the fatigue properties of PBF-EB-produced Ti-6Al-4V alloys are improved following the HIP process, due to a reduction in defect size, which is detrimental to fatigue life [11]. HIPped Ti-6Al-4V alloys absorbed more energy than as-built samples during the Charpy test, due to lower porosity and increased α lath thickness [12]. HIP treatment can also alter the phase composition, size, and texture of PBF-EB samples. Lu et al. demonstrated that HIPping (920 °C for 2 hours at 100 MPa in argon) eliminated all residual martensite, increased the α lath thickness, and intensified the texture component of $\langle 0002 \rangle$ in the α-phase [13]. While HIPping benefits fatigue properties, the potential reduction in static strength due to the coarser microstructure should also be considered [14, 15]. Nandwana et al. applied HIP at supertransus temperatures followed by rapid quenching as an alternative to the standard HIP process. The results showed that samples treated at supertransus temperatures and rapidly quenched exhibited higher tensile strength than standard HIPped samples. The supertransus HIP process reduced mechanical anisotropy by transforming the columnar primary β structure into equiaxed β grains and modifying the associated α texture [16].

Heat treatments of Ti-6Al-4V alloys can be categorized into three main temperature ranges: subtransus, near-transus, and supertransus. Sub-transus and near-transus heat treatments do not significantly affect the columnar primary β structure. However, super-transus temperatures completely transform the β columns into equiaxed grains. Sub-transus and near-transus treatments primarily affect α-lath size and morphology [17]. Syed et al. reported in [18] that samples heat-treated at 920 °C for 2 hours and air-cooled displayed 25 % higher ductility and 7 % lower yield and tensile strength compared to as-built PBF-EB samples, due to α lath coarsening. In heat treatments applied to Ti-6Al-4V alloys, not only temperature but also time and cooling conditions play a crucial role. Galarraga et al. annealed as-built samples at varied temperatures (600, 700, and 800 °C) and time periods ranging from 10 to 120 hours. Increasing both temperature and time increased α-lath thickness [19]. Their previous work investigated the effects of different cooling conditions (furnace, air, and water quenching) following super-transus heat treatment. According to their results, the cooling rate significantly affected both the microstructure and the mechanical properties. As the cooling rate increased, hardness, yield strength, and tensile strength also increased. However, ductility decreased dramatically due to the formation of an α'-martensitic structure [9].

Some researchers have applied aging treatments to PBF-EB-produced parts and investigated the effects of aging on microstructure and mechanical behavior. An aging step is typically included to promote the decomposition of α' or retained β phases in the microstructure [20]. Zhai et al. used a procedure that involved solutionizing at 950 °C for 1 hour, water-quenching to room temperature, aging at 500 °C for 7 hours, and air-cooling. This secondary process significantly improved the fracture toughness [21]. Car-

roza et al. aged the material at 540 ℃ for 4 hours after supertransus annealing, using both furnace cooling and water quenching. For the furnace-cooled, solution-treated samples, aging resulted in a slight increase in both strength and ductility, attributable to a reduced β-phase fraction and α-coarsening. On the other hand, in the water-quenched samples, aging led to a slight decrease in strength but a significant increase in ductility, attributed to grain coarsening [22]. Soundarapandiyan et al. applied HIP, solution treatment, and aging to Ti-6Al-4V parts and showed that these post-fabrication treatments homogenized the microstructure, reduced pore quantity, and improved impact resistance and fatigue life. However, strength was reduced due to α coarsening [23].

Although studies have examined post-thermal treatment of Ti-6Al-4V alloy produced by PBF-EB, they remain limited in scope and depth. Therefore, this study aims to elucidate and better understand the impact of aging temperature (500–600 ℃) and time (4–10 hours) on solution-treated Ti-6Al-4V alloys produced through PBF-EB. Additionally, the study investigates the effect of HIP temperature (800, 920, and 1050 ℃) on the microstructure and mechanical properties of these alloys.

2. Materials and methods

In this study, the PBF-EB samples were fabricated using an ARCAM A2X system. The machine was operated with standard parameters for Ti-6Al-4V, as recommended by the manufacturer (*software version 5.0.61 Theme*). The samples were built with a layer thickness of 50 µm, a maximum beam power of 3 kW, and an accelerating voltage of 60 kV. The speed function was set to 45. The beam speeds for preheating, contour scanning, and hatching were 10, 140, and 9 m s^{-1}, respectively. Their corresponding focus offsets were 70, 6, and 25 mA, respectively.

The Ti-6Al-4V powder used in this study has a particle-size distribution with $D10 = 51$ µm, $D50 = 73$ µm, and $D90 = 105$ µm. Particle size analysis of three powder samples was performed using laser diffraction in accordance with ASTM B822 [24]. Powder flowability, measured with a Hall flowmeter funnel, was 24.85 s/50 g following ASTM B213 [25]. The powder was investigated using a Scanning Electron Microscope (SEM) to reveal its particle morphology. As shown in Fig. 1a, the Ti-6Al-4V powder particles are predominantly spherical. The powder was cold-mounted in epoxy resin and prepared through standard metallographic techniques of sectioning, grinding, and polishing to examine cross-sectional porosity. As visible in Figure 1b, some particles contain internal voids.

The nominal chemical composition of the Ti-6Al-4V powder, as provided by the supplier (ARCAM), is listed in Table 1. To examine the effect of part orientation, samples were produced both horizontally and vertically, as shown in Fig. 2.

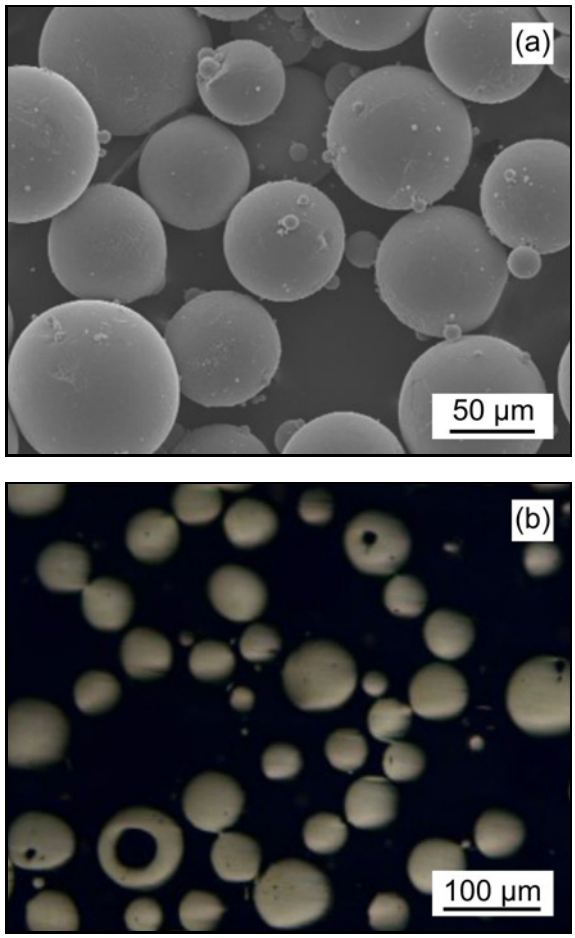

Fig. 1. (a) SEM image of powder particles and (b) OM image of powder particle cross-sections.

Table 1. Chemical composition of powder feedstock (wt.%)

Al	V	C	Fe	O	N	H	Ti
4	6	0.03	0.1	0.15	0.01	0.003	Balance

After the production stage, the samples were separated from the base plate using an EDM wire machine. The samples were divided into two groups for post-processing: one group underwent heat treatment (conditions detailed in Table 2), and the other group was processed via hot isostatic pressing (HIP parameters outlined in Table 2). All aged samples were solution-treated (HT1) before aging.

The microstructures of as-built, heat-treated, and HIPped samples were investigated using an optical

Table 2. Heat treatment and HIP test plan (AC: Air cooling, FC: Furnace cooling)

Heat treatment	Time (min)	Temperature (℃)	Cooling	Pressure (MPa)
HT1 (ST)	30	950	FC	–
HT2 (AG)	240 (4 h)	500	AC	–
HT3 (AG)	240 (4 h)	550	AC	–
HT4 (AG)	600 (10 h)	500	AC	–
HT5 (AG)	600 (10 h)	550	AC	–
HT6 (AG)	600 (10 h)	600	AC	–
HIP1	120 (2 h)	800	FC (30 K min^{-1})	200
HIP2	120 (2 h)	920	FC (30 K min^{-1})	100
HIP3	120 (2 h)	1050	FC (30 K min^{-1})	100

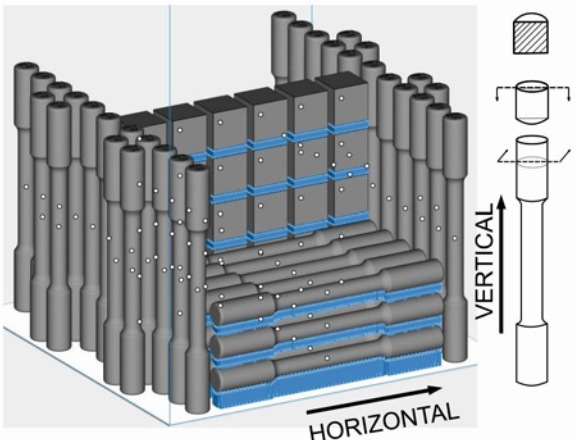

Fig. 2. Sample layout in process chamber and cutting planes for metallographic specimen preparation from tensile samples.

microscope (OM). Metallographic investigation samples were prepared by cutting the tips of the tensile specimens, as illustrated in Fig. 2. Before microstructural analysis, the samples were ground with 1000 and 2500-grit SiC paper and polished with 1 μm diamond slurry. Finally, all the samples were finished with colloidal silica suspension. To reveal the grain structure and phases within the microstructures, a solution of 91 ml of water, 6 ml of HNO_3, and 3 ml of HF (Kroll's reagent) was used as the etchant and applied to the surfaces.

Quantitative analysis of microstructural images was performed using the FIJI software package. The relative density was measured from optical micrographs using quantitative image analysis. For each sample condition, five optical micrographs were taken at random locations on the polished cross-section to ensure statistical representation. These images were converted to binary format using FIJI, in which pores were distinguished from solid material using contrast thresholding. The porosity fraction was calculated for each image. The average relative density and its standard deviation were then determined from these five measurements per condition. The interlamellar spacing of the α phases was measured using the intersection method, as described in [9]. The intersection method was applied by randomly superimposing a circular test grid of known radius R onto the micrograph. The number of intersections between the α lamellae and the test line, denoted as M, was recorded. The number of intersections per unit length was calculated using the relation $N_\mathrm{L} = 2\pi R/M$. The mean random spacing was obtained as the reciprocal of this value, $\sigma_\mathrm{r} = 1/N_\mathrm{L}$. Subsequently, the mean true spacing was determined by halving the mean random spacing, yielding $\sigma_\mathrm{t} = \sigma_\mathrm{r}/2$. The analysis was performed on five images for each condition, and the values were averaged to determine the interlamellar spacing of the α phase for each condition. The relative density of the samples was also measured using image analysis.

The samples were qualitatively analyzed using a Rigaku Miniflex 600 X-ray diffractometer with CuKα radiation (λ = 1.540562Å), operated at 40 kV and 15 mA, with a scanning rate of 2° min^{-1}. Following the procedure outlined in Fig. 2 for metallographic samples, the XRD specimens were sectioned, and their analysis surfaces were ground with 1000-grit SiC paper.

Tensile tests were performed using a tensile testing machine at a crosshead speed of 1 mm min^{-1}, in accordance with ASTM E8 [26]. Tensile testing was performed using three samples per condition. The tensile test specimens were machined to improve surface quality before testing.

3. Results and discussion

The following section analyzes the effects of heat treatments and HIP processes on the microstructure and mechanical properties of PBF-EB Ti-6Al-4V. Figure 3 shows the OM images of as-built samples. Figures 4 and 5 present OM images of heat-treated and hot-isostatically pressed samples, acquired horizontally and vertically. All samples contained pores. The morphology of these pores is generally circular, with

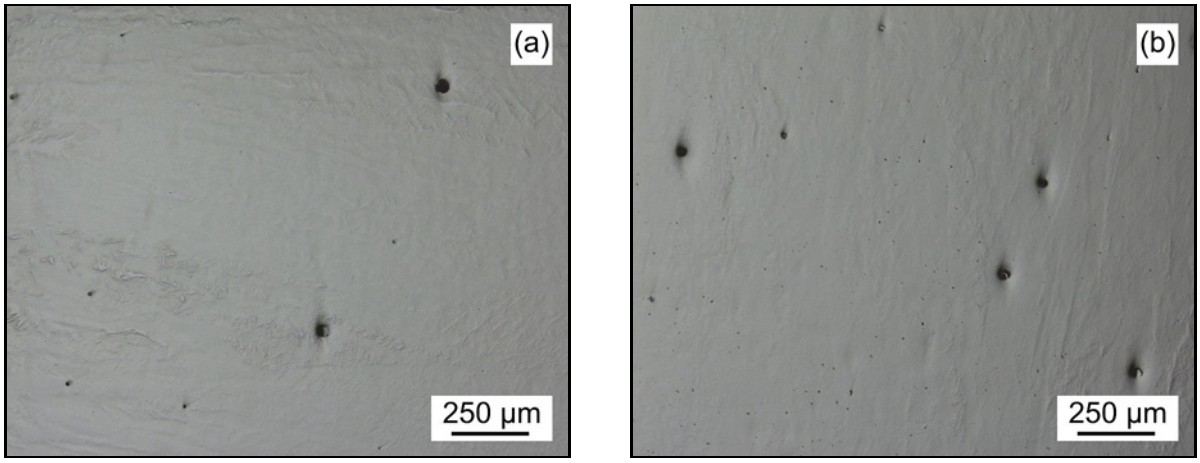

Fig. 3. OM images of as-built samples: (a) horizontally built and (b) vertically built.

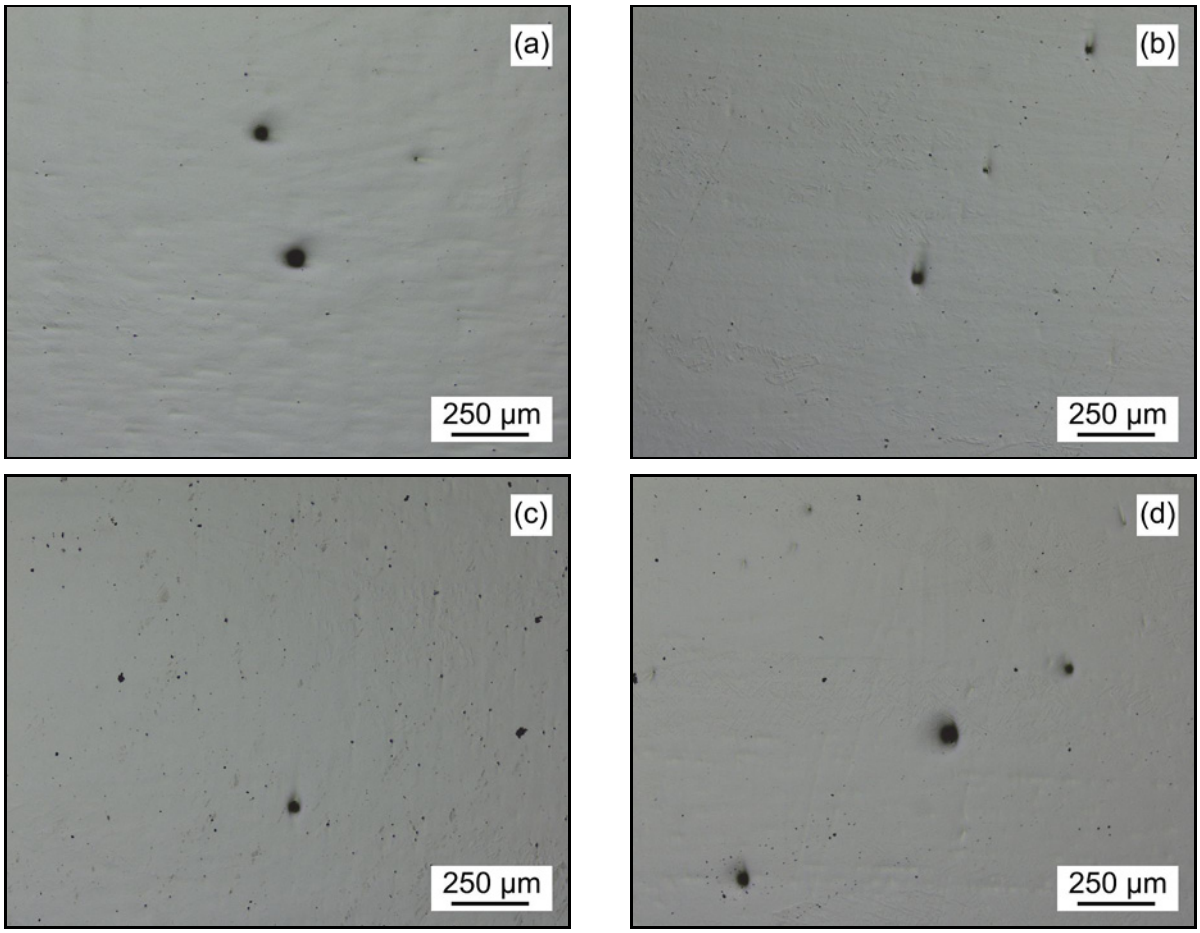

Figs. 4a–d. OM images of the samples horizontally built: (a) HT1, (b) HT2, (c) HT3, (d) HT4.

diameters ranging from 1.5 to 82 µm. These porosities are likely related to the stock material, which contains gas porosities inherited from the powder production method. Moreover, the number of pores is significantly higher in vertically produced samples, resulting in a lower density than in horizontally produced samples (Table 3). In literature, the relationship between defect formation and build orientation is controversial. Some researchers have reported that porosities are more frequently observed in horizontally built samples due to higher cooling rates [27]. De Farmanoir et al. also reported a higher prevalence of irregularly shaped defects in horizontally built samples, attributed to longer scan lengths and higher cooling rates [28]. On

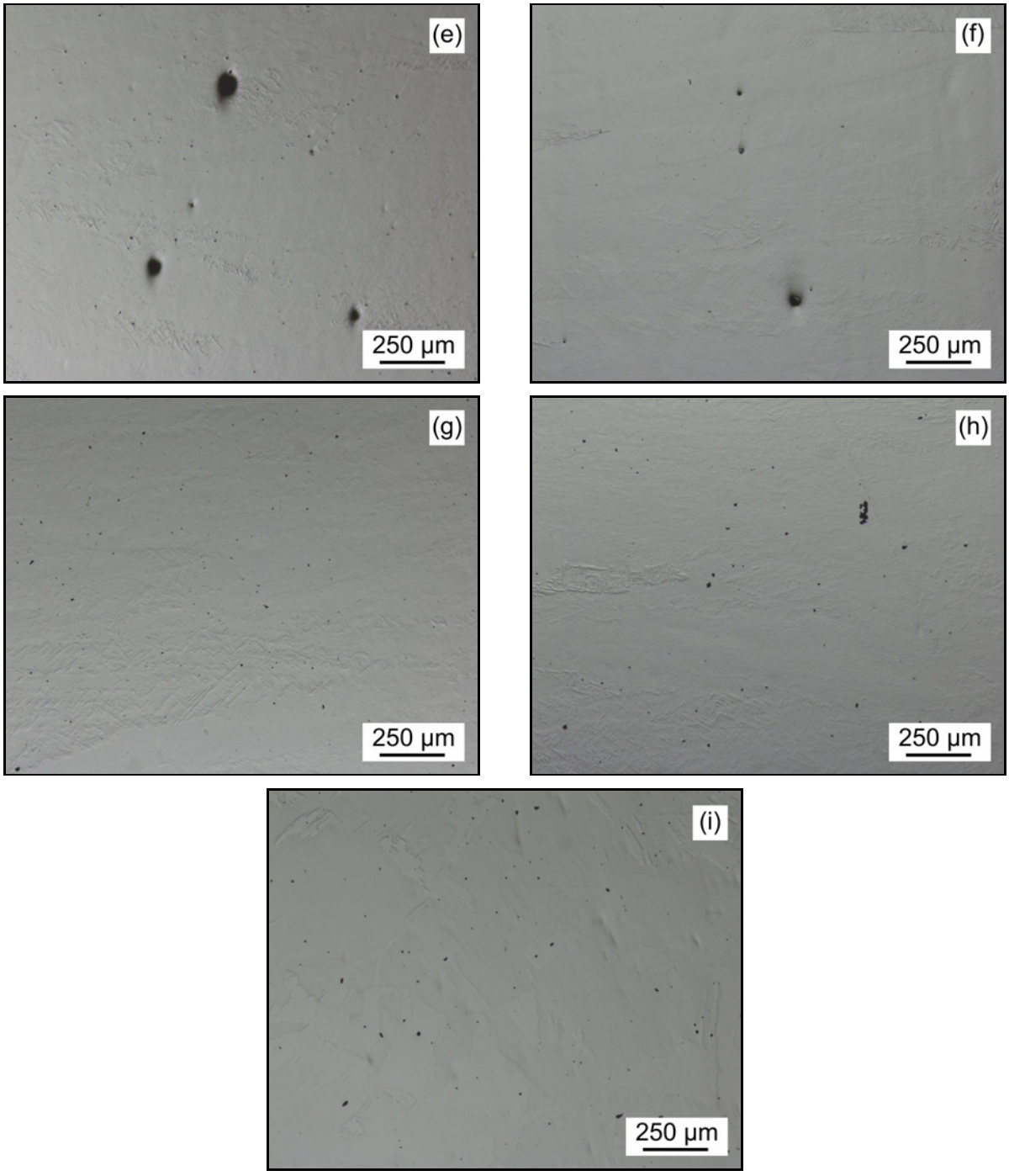

Figs. 4e–i. OM images of the samples horizontally built: (e) HT5, (f) HT6, (g) HIP1, (h) HIP2, and (i) HIP3.

the other hand, a higher number of spherical pores were detected in horizontally built parts, whereas vertically built parts had a greater number of lack-of-fusion defects [29]. Additionally, lack-of-fusion defects were more frequently observed on the fracture surfaces of vertically oriented tensile test specimens [30]. Although no irregularly shaped lack-of-fusion defect was detected in our case, the higher porosity observed in the vertical samples can be attributed to increased cooling rates. As shown in Fig. 2, vertical samples were built directly on the baseplate without support structures, whereas horizontal samples were constructed on supports. The low-density nature of the support structures may have reduced thermal conductivity between the horizontal samples and the baseplate. This reduced heat transfer to the baseplate, prolonging the melt pool duration. The extended melt pool lifetime allowed more time for gas pores to escape before solidification. Another important factor to consider is the placement of the vertical and horizontal

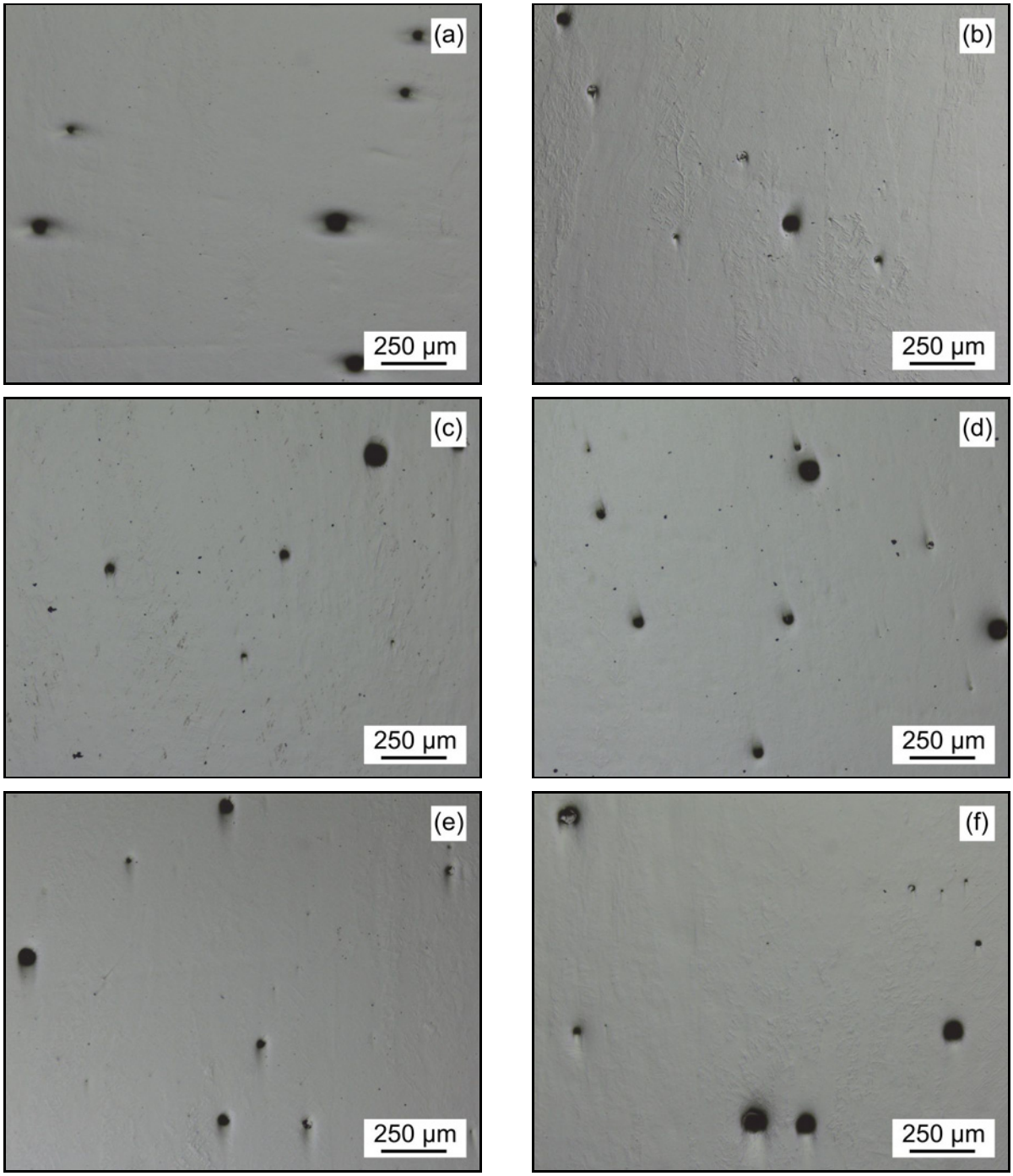

Figs. 5a–f. OM images of the samples vertically built: (a) HT1, (b) HT2, (c) HT3, (d) HT4, (e) HT5, (f) HT6.

samples within the production chamber. According to the production plan, vertical samples were placed on the chamber exterior, whereas horizontal samples were placed on the interior. Hrabe et al. suggested that increased electron-beam deflection could result in a cooler exterior within the build space, potentially leading to higher cooling rates than the interior [31]. They anticipated that samples produced in the exterior region of the process chamber would exhibit a finer microstructure and greater strength. Their findings indicated that part location exerts an influence of less than 3 %, potentially due to secondary thermal mass effects. Galarraga et al. also examined the effect of part location and found no significant differences in the microstructures of samples produced at the center versus those at the edge of the build platform. Interestingly, contrary to expectations of higher porosity and a finer microstructure in the outer parts, they observed that the interior samples had higher porosity and a finer mi-

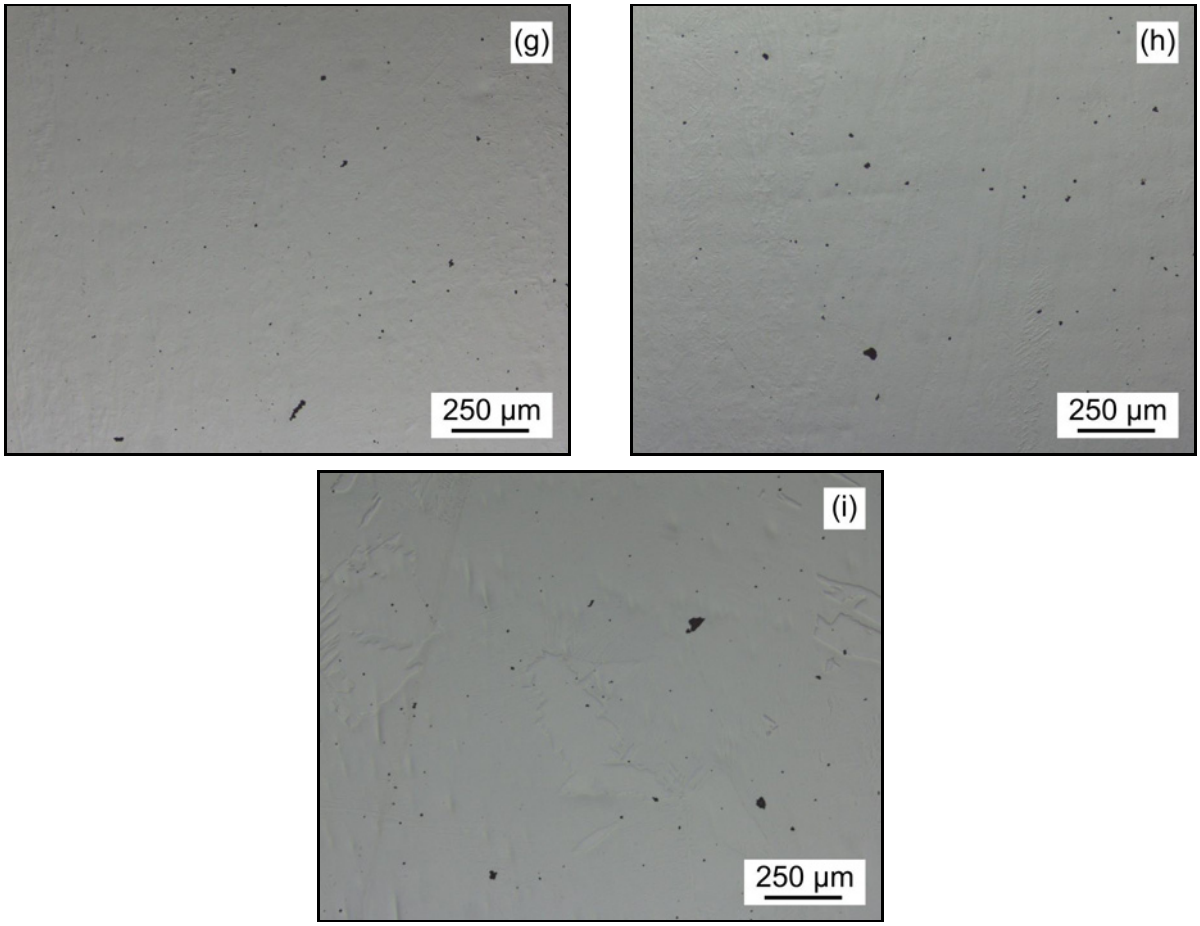

Figs. 5g–i. OM images of the samples vertically built: (g) HIP1, (h) HIP2, and (i) HIP3.

Table 3. Average porosity and α-lath size measurements with standard deviations

Sample condition	Porosity (%)		α-lath thickness (µm)	
	Horizontal	Vertical	Horizontal	Vertical
As-built	99.71 ± 0.21	99.56 ± 0.16	1.7 ± 0.2	1.4 ± 0.16
HT1	99.63 ± 0.25	99.27 ± 0.33	2.21 ± 0.24	1.98 ± 0.22
HT2	99.65 ± 0.15	99.53 ± 0.2	2.51 ± 0.42	2.22 ± 0.47
HT3	99.5 ± 0.15	99.41 ± 0.13	2.68 ± 0.58	2.22 ± 0.43
HT4	99.6 ± 0.07	99.14 ± 0.25	2.69 ± 0.71	2.15 ± 0.5
HT5	99.55 ± 0.11	99.35 ± 0.06	2.43 ± 0.46	2.12 ± 0.46
HT6	99.57 ± 0.26	99.35 ± 0.27	2.55 ± 0.41	2.04 ± 0.33
HIP1	99.86 ± 0.02	99.81 ± 0.03	1.77 ± 0.31	1.54 ± 0.18
HIP2	99.83 ± 0.04	99.79 ± 0.03	2.74 ± 0.38	2.34 ± 0.49
HIP3	99.8 ± 0.03	99.75 ± 0.01	2.85 ± 0.72	2.36 ± 0.36

crostructure [19]. Although the existing literature suggests minimal effects of part location, it remains crucial to consider its potential influence on porosity.

Having established the baseline porosity characteristics, the analysis now turns to the efficacy of post-processing in mitigating these defects. HIP processes effectively enhanced density, while heat treatments did not. All HIP cycles substantially reduced pore size and nearly closed all pores. The HIP1 process, conducted at 800 ℃ under a higher pressure of 200 MPa, achieved the highest relative density (99.86 %), underscoring its superior effectiveness in increasing material density. The cycle (800 ℃/200 MPa) also eliminated the density difference between samples fabricated in different directions.

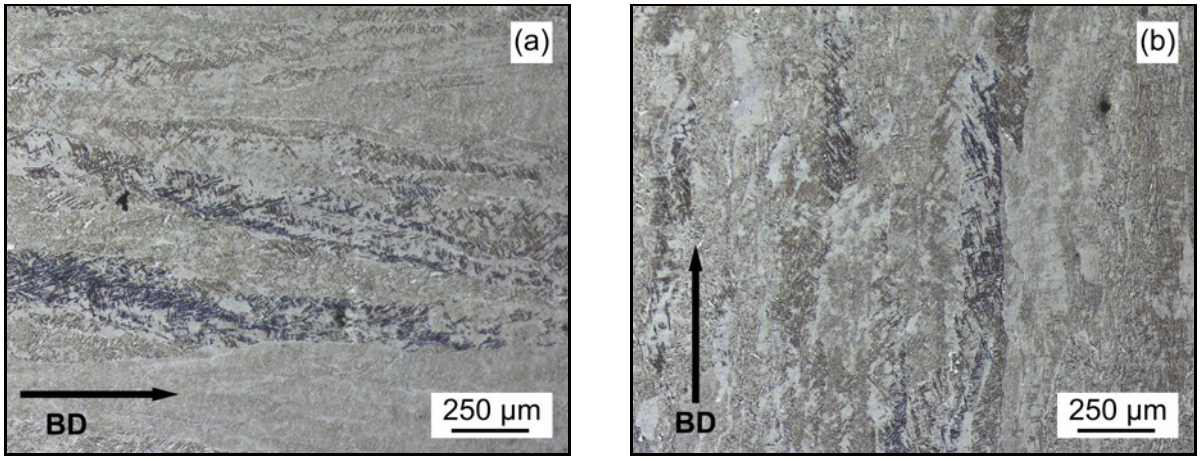

Fig. 6. OM images of etched surfaces: (a) horizontally and (b) vertically as-built samples.

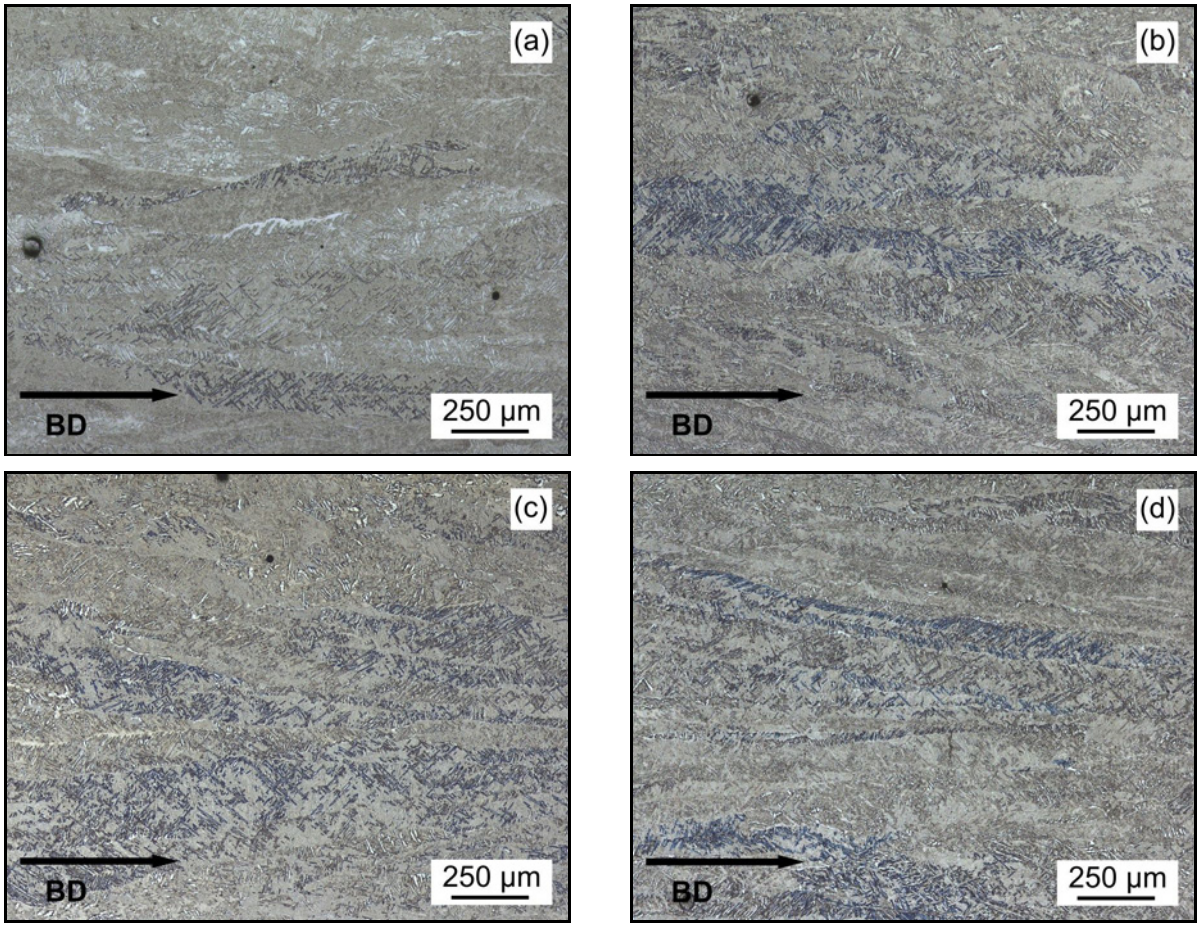

Figs. 7a–d. OM images of the etched samples horizontally built: (a) HT1, (b) HT2, (c) HT3, (d) HT4.

Beyond porosity reduction, the HIP and heat treatment processes also induced significant microstructural transformations. In Figs. 6, 7, and 8, the etched microstructures reveal that all samples retained the columnar primary β structure from the PBF-EB process, except for the HIP3 samples. A noteworthy observation is that in vertically oriented samples, the primary β columns align parallel to the tensile direction, whereas in horizontally oriented samples, the columns are oriented perpendicular to it. This columnar structure arises from β-grain nucleation on the top surface of the prior layer, followed by epitaxial growth perpendicular to the molten pool during additive manufacturing [6]. Previous studies have indicated that heat treatments and HIP processes conducted below the transus typically preserve the microstructure of

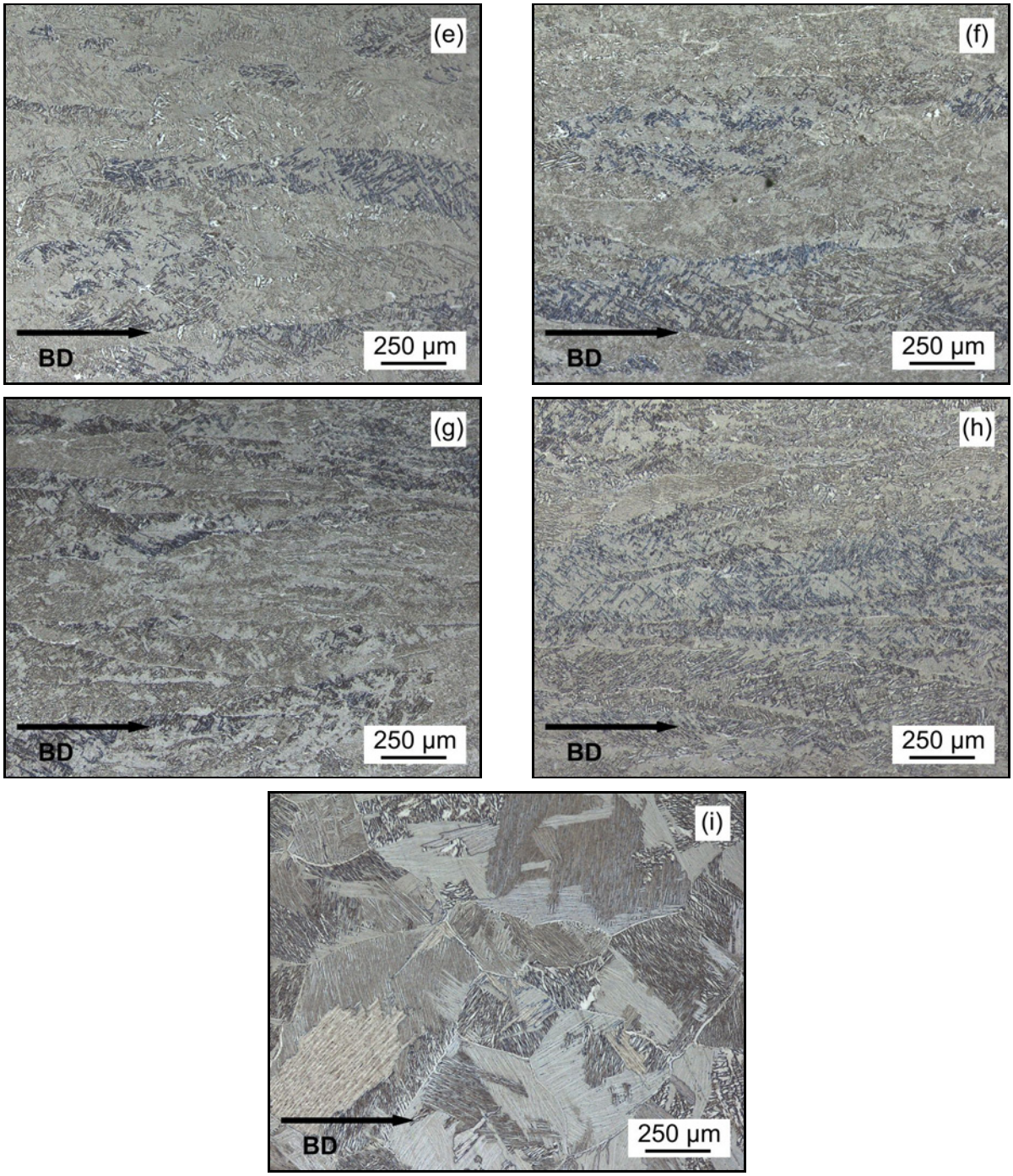

Figs. 7e–i. OM images of the etched samples horizontally built: (e) HT5, (f) HT6, (g) HIP1, (h) HIP2, and (i) HIP3.

the PBF-EB process. However, secondary processes applied at temperatures above the transus transform the microstructure from columnar to equiaxed [18, 19, 32, 33]. An essential finding of this study is the transformation behavior of primary β phases following HIP at supertransus temperatures. After supertransus HIP (HIP3), the columnar primary β phases entirely transformed into an equiaxed form, in horizontally produced samples. Vertically built samples exhibited a more complex phase response than horizontally built samples. Their columnar structure largely persisted, but some grains underwent significant thickening and a partial transition to an equiaxed morphology. This outcome can be attributed to the long-axis orientation parallel to the production direction in vertically fabricated samples, which leads to the formation of more extended β columns. The inherent alignment promotes the formation of elongated columnar structures. Consequently, these longer β columns may require prolonged exposure or higher temperatures for complete

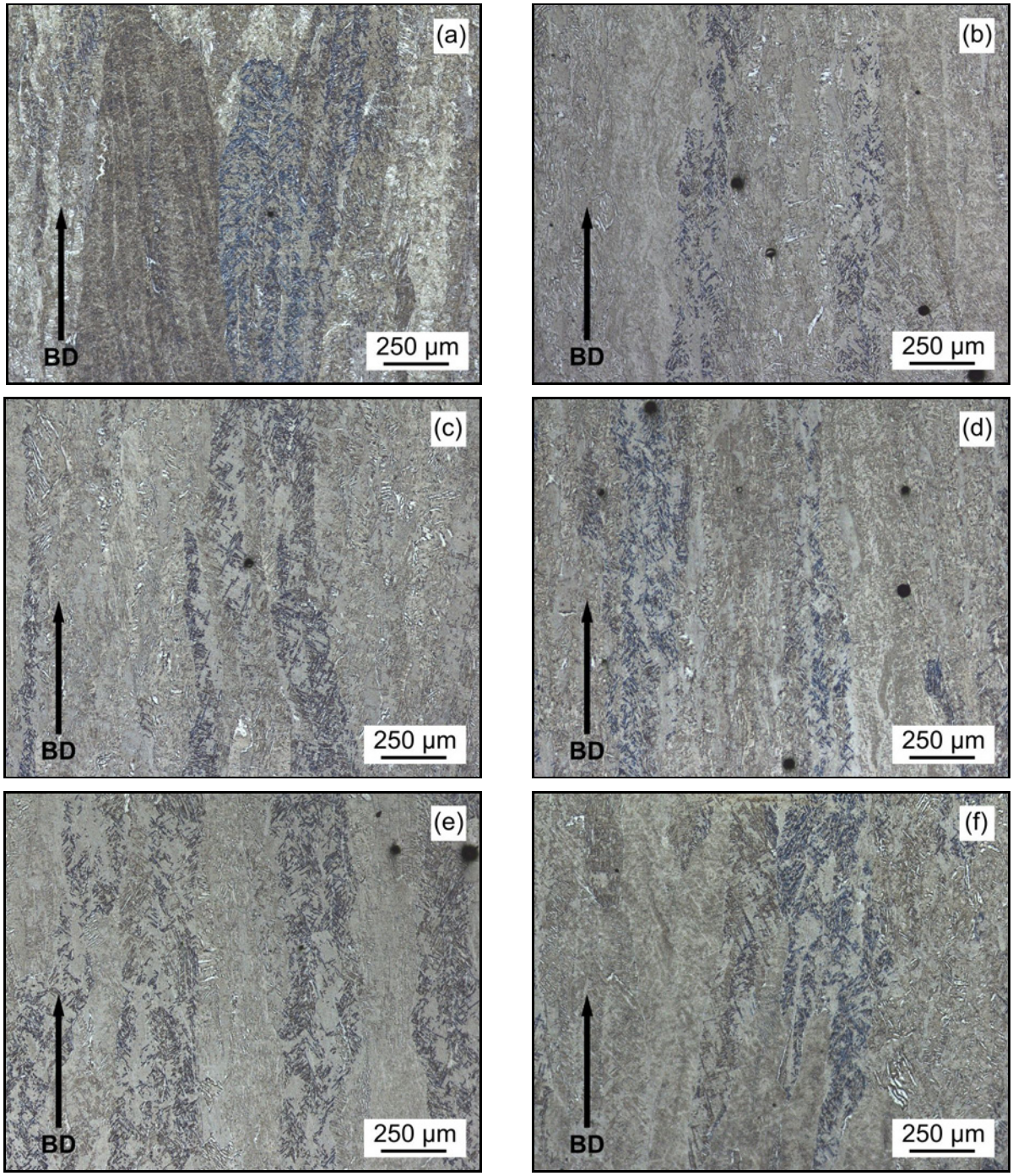

Figs. 8a–f. OM images of the etched samples vertically built: (a) HT1, (b) HT2, (c) HT3, (d) HT4, (e) HT5, (f) HT6.

transformation into equiaxed grains during HIP.

To comprehend the impact of heat treatments on the microstructure at a finer scale, higher magnification OM images (Figs. 9–11) reveal the $\alpha+\beta$ lamellar structure. Vertically built as-built samples possessed finer α laths than horizontally built samples (Table 3), due to higher cooling rates [34, 35]. Solution heat treatment increased α-lath thickness, and subsequent aging further amplified this growth, although variations in aging parameters had no significant effect.

The phase evolution suggested by the microstructural observations was further investigated using XRD. The XRD analysis of the as-built samples confirmed the presence of both α and β phases under both horizontal and vertical production conditions (Fig. 12). It is important to note that XRD intensities can be influenced by strong crystallographic texture, particularly in additively manufactured materials. Nonetheless, the vertically built as-built specimens exhibited a more pronounced β peak, indi-

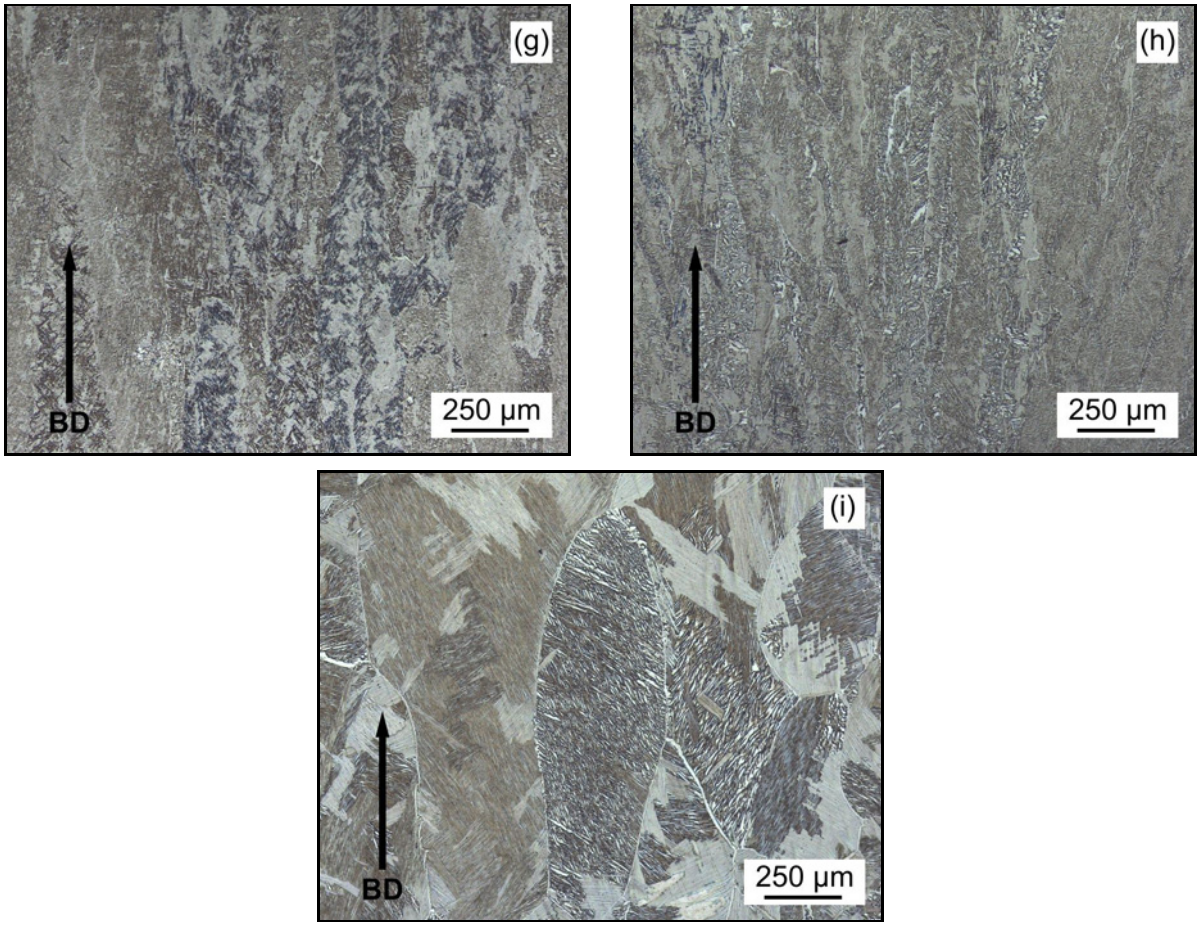

Figs. 8g–i. OM images of the etched samples vertically built: (g) HIP1, (h) HIP2, and (i) HIP3.

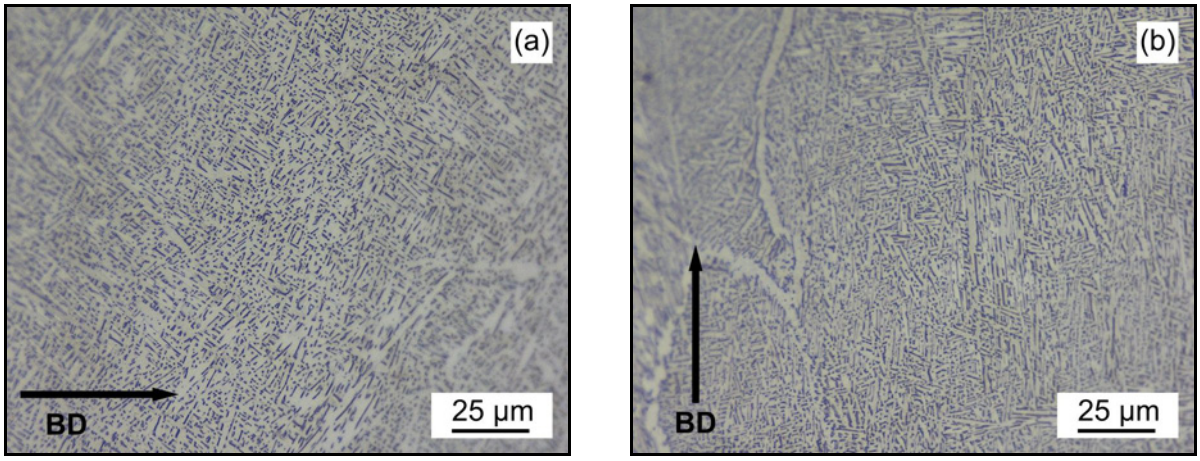

Fig. 9. OM images of etched surfaces: (a) horizontally and (b) vertically as-built samples.

cating a higher retained β-phase fraction than the horizontally built samples. For horizontally oriented specimens, solution heat treatment increased the relative intensity of the (0002) α reflection, indicating a stronger α-phase texture after solution heat treatment. The β peak also became more pronounced in these samples, indicating an increase in detectable β-phase content. This behavior is consistent with observations reported by Shui et al. [32], who found that solution treatment at 920 °C, followed by furnace cooling, increased the β-phase fraction and α-texture intensity in PBF-EB Ti-6Al-4V alloys. XRD analysis revealed notable differences between the solution-treated horizontally and vertically built samples. In the vertically built samples, no discernible β peak was detected after solution treatment, indicating a signifi-

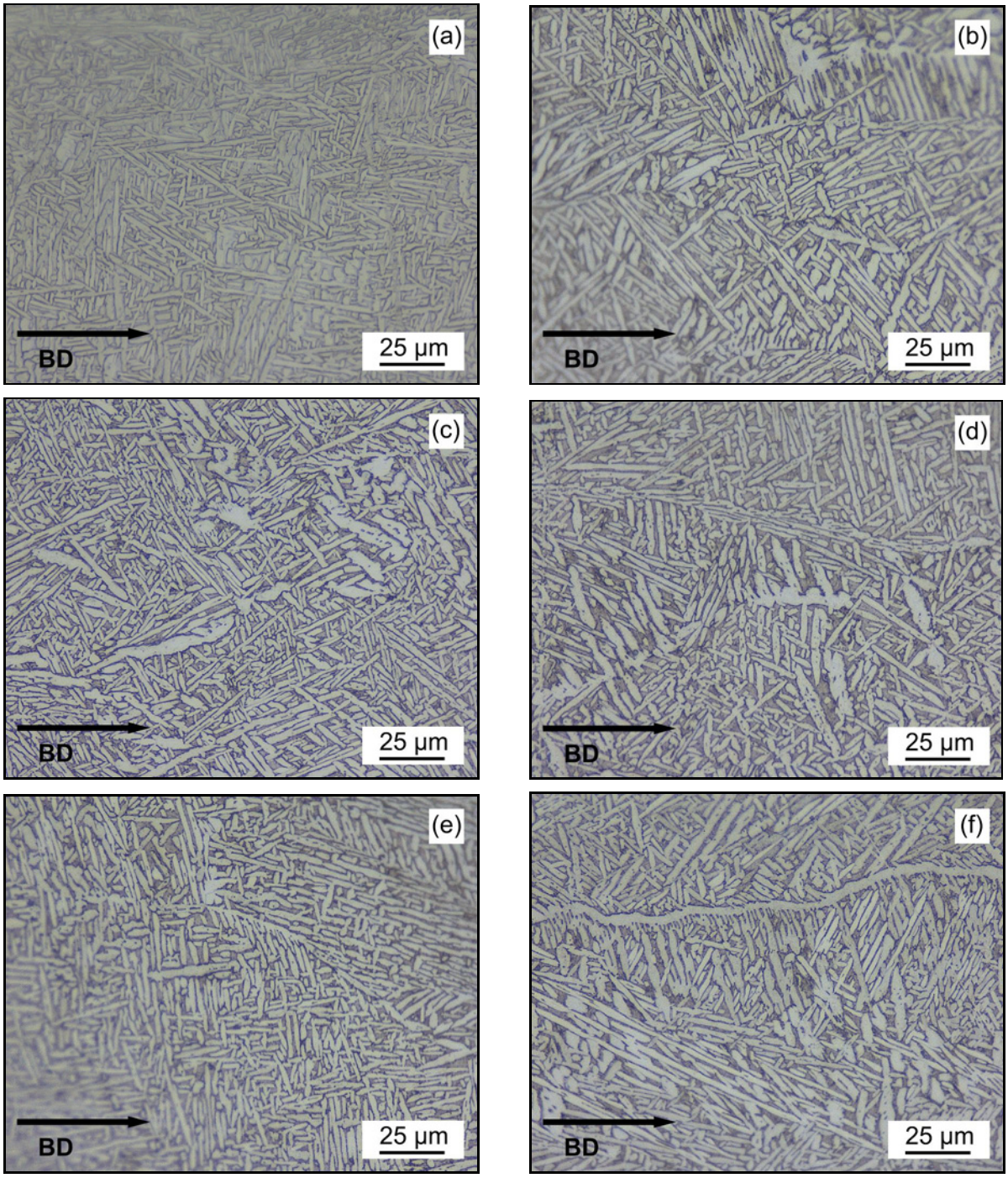

Fig. 10. OM images of the etched samples horizontally built: (a) HT1, (b) HT2, (c) HT3, (d) HT4, (e) HT5, and (f) HT6.

cantly reduced β-phase content. Although texture can strongly influence peak intensity, the complete disappearance of this peak, along with the entire (0002) α-phase peak, indicates a major alteration in phase composition and orientation. Aging treatments with shorter durations and lower temperatures (HT2, HT3, and HT4) in the horizontally built samples resulted in a reduced β-phase peak, suggesting potential decomposition of retained β and increased α-phase content. In contrast, no significant changes were observed in the vertically built samples under the same aging conditions. However, longer-time, higher-temperature aging (HT5 and HT6) resulted in the emergence of noticeable β-phase peaks, with this effect being more pronounced in vertically built samples. This indicates that higher temperatures and extended aging may substantially increase β-phase content, particularly in vertically oriented builds. Another significant finding

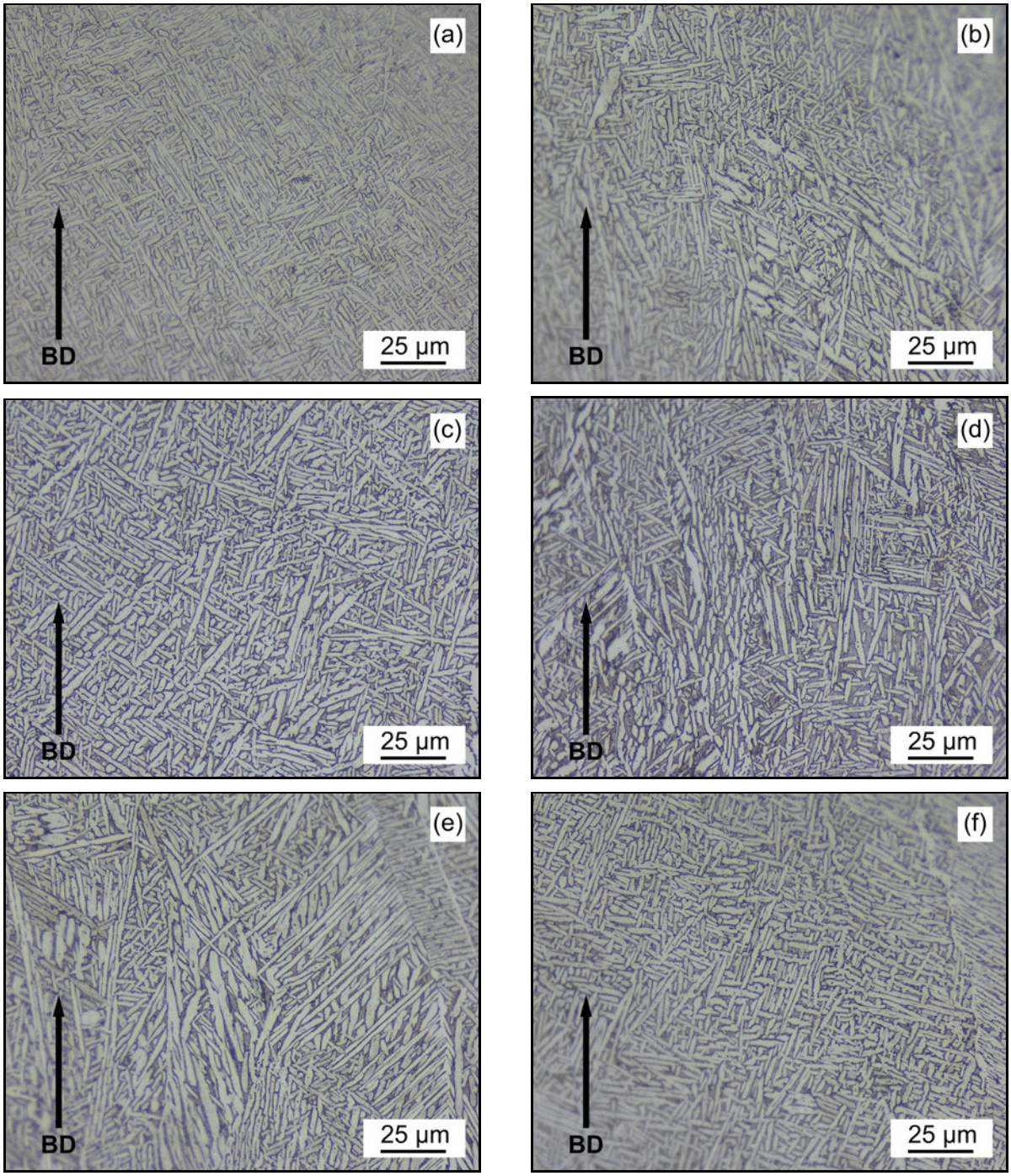

Fig. 11. OM images of the etched samples vertically built: (a) HT1, (b) HT2, (c) HT3, (d) HT4, (e) HT5, and (f) HT6.

was the absence of any Ti_3Al (α_2) phase peaks in the aged samples, indicating that precipitation did not occur.

These microstructural and phase characteristics directly govern the mechanical properties, as revealed by tensile testing. The tensile test results revealed a significant difference in strength between build orientations (Fig. 13). Horizontally built samples exhibited an average yield strength of 942 MPa and a tensile strength of 1014 MPa, whereas vertically built samples reached 924 and 986 MPa, respectively. Although the vertically oriented samples exhibited a finer α-lath structure, the horizontally oriented specimens exhibited higher yield and ultimate tensile strength, suggesting the influence of an additional strengthening mechanism. This discrepancy in mechanical properties may be attributed to the higher β-phase content present in the vertically built samples. The β phase, characterized by its body-centered cubic (bcc) structure with multiple slip systems, tends to be softer

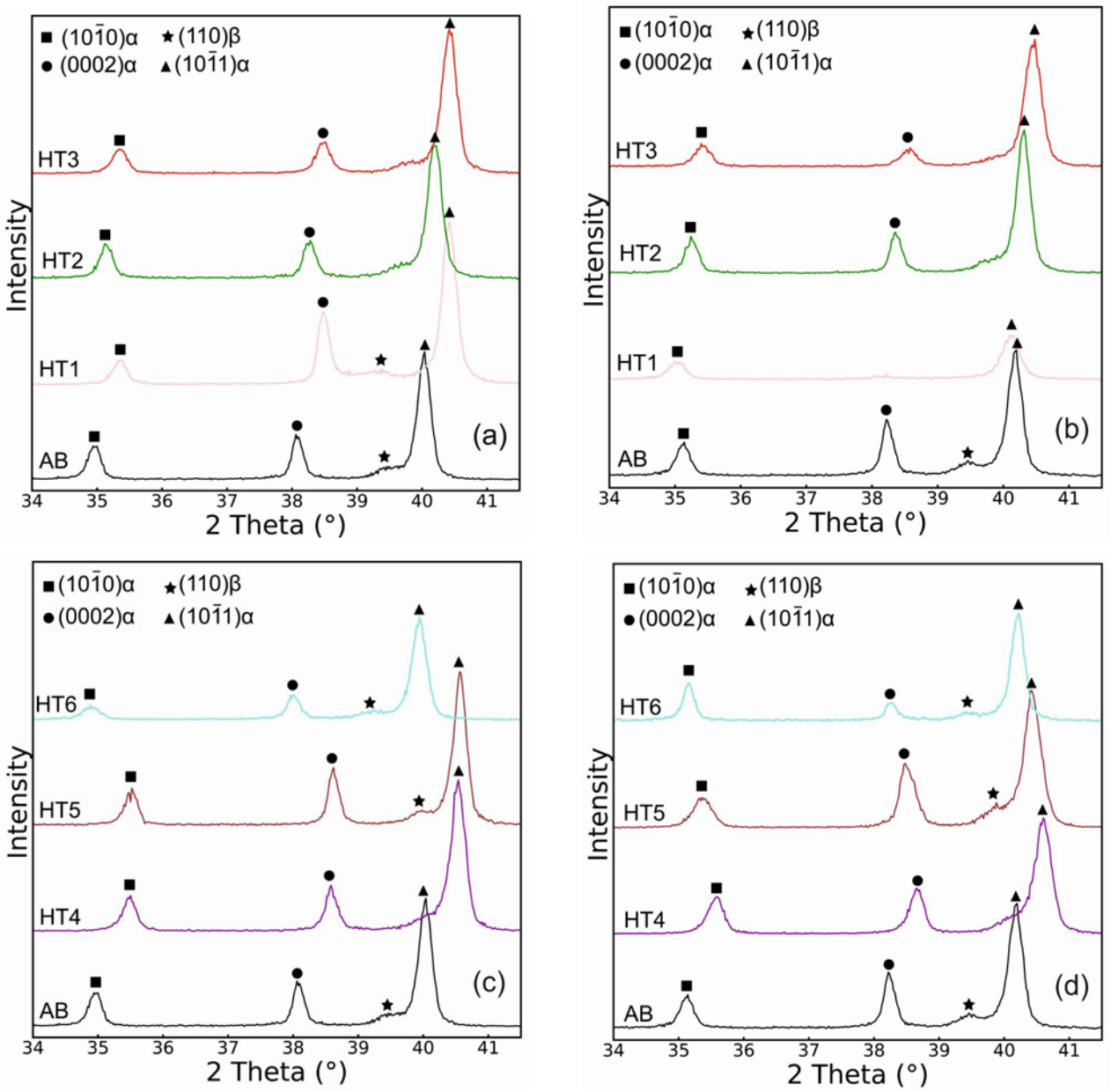

Fig. 12. XRD result of the heat-treated samples: (a) horizontally as-built-HT1-HT2-HT3, and (b) vertically as-built-HT1-HT2-HT3, (c) horizontally as-built HT4, HT5, HT6, and (d) vertically as-built-HT4-HT5-HT6

than the hexagonal close-packed (hcp) α phase. Consequently, the higher β-phase fraction in vertically built samples could reduce overall strength, explaining their lower YS and UTS than those of horizontally built samples. This observation aligns with the established understanding of phase contributions in Ti-6Al-4V alloys, in which the β phase imparts ductility but may compromise strength relative to the harder α phase [36].

Following solution treatment, the strength values of both vertically and horizontally built samples decreased to some extent (9 % yield strength and 4 % ultimate tensile strength reductions for vertically built samples, and 13 % yield strength and 6 % ultimate tensile strength reductions for horizontally built samples), possibly due to α coarsening. The relatively higher strength of vertically built and solution-treated (HT1) samples can be attributed to their lower β-phase content, finer α-lath thickness, and textural evolution.

Aging processes appear to compensate for the decrease in strength observed after solution treatment. The strengthening effect of aging is associated with the decomposition of the metastable β phase and an increase in the α phase content. With aging, the proportion of the harder α phase in the microstructure

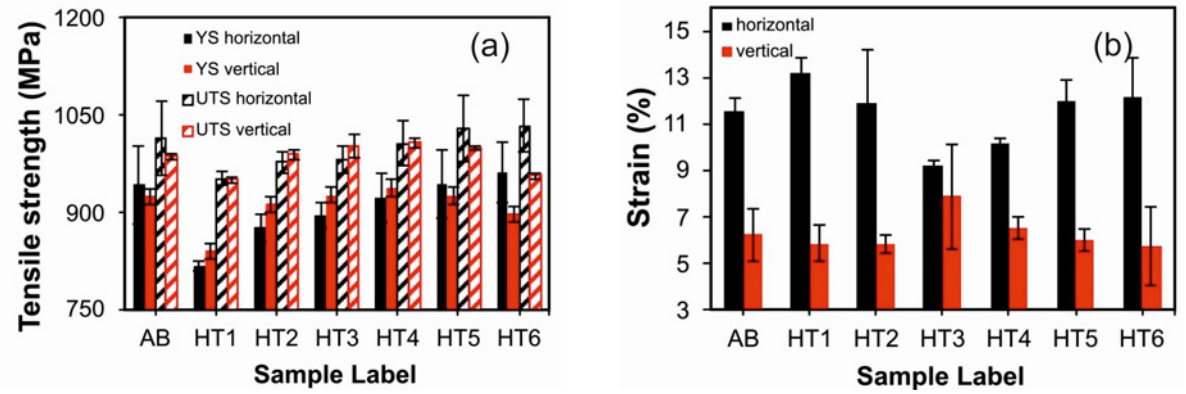

Fig. 13. Tensile test results of as-built and heat-treated samples: (a) yield and ultimate tensile strength and (b) elongation to fracture.

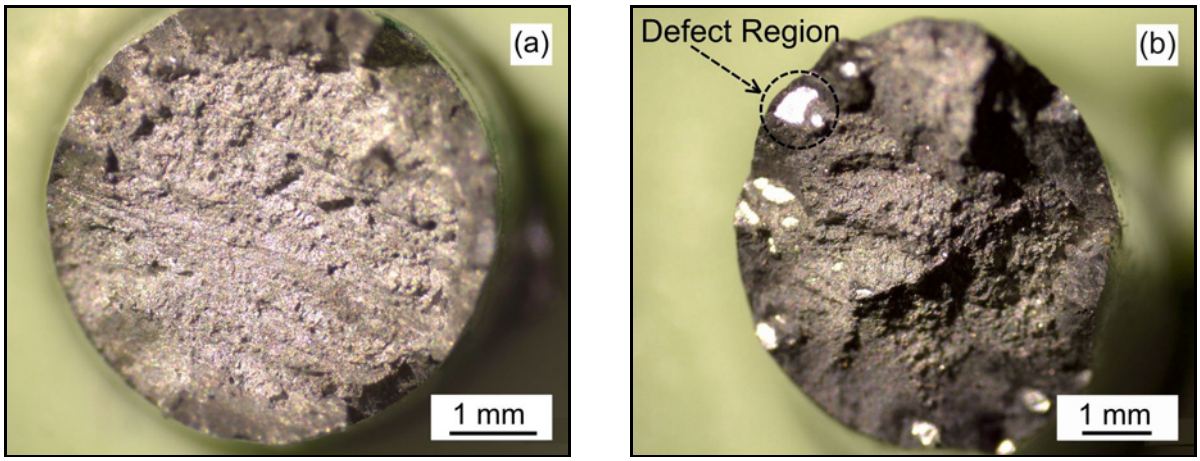

Fig. 14. Fracture surfaces of as-built samples: (a) horizontally built and (b) vertically built.

increases, thereby increasing strength. The results of this study are consistent with findings from another study in which solution treatment and aging heat treatments were applied after PBF-EB [22]. The increase in strength with aging also suggests the formation of precipitates, such as Ti_3Al (α_2). However, this possibility is considered weak, as the formation of this phase during aging requires the aluminum content of the alloy to exceed a critical value (> 6 wt.%) [37, 38]. Moreover, no Ti_3Al (α_2) related peaks were detected in the XRD pattern of the aged sample, further supporting the low likelihood of Ti_3Al (α_2) formation. Several studies have applied solution treatment and aging to Ti-6Al-4V alloys produced by additive manufacturing and have observed the formation of the Ti_3Al phase by XRD and electron microscopy [39–41]. However, although selective laser melting was used in these studies, no evidence of this phase has been reported in the literature on the effects of solution treatment and aging heat treatments on Ti-6Al-4V alloys after PBF-EB. It is well known that the PBF-EB process must be conducted under vacuum. The vacuum lowers the evaporation temperature of aluminum, facilitating its vaporization [42]. This reduction in aluminum content may explain the inability to observe the formation of the Ti_3Al phase during solution treatment and aging. When subjected to excessively high aging temperatures and longer durations (HT5 and HT6), vertically built samples experienced a decrease in strength. This reduction in strength is likely linked to the increased β-phase fraction, as indicated by XRD, which suggests that the higher β content could contribute to the overall weakening of the material.

Heat treatments did not significantly affect the percentage elongation. However, horizontally built samples exhibited greater ductility in both the as-built and heat-treated conditions. This can be attributed to the lower porosity content in the horizontally built samples, which likely contributed to improved elongation during tensile testing.

Fracture surface analysis provided further insight into the ductile behavior. The examination of fracture surfaces revealed notable differences between the vertically produced, as-built sample (Fig. 14) and the heat-treated samples (Figs. 15 and 16). In these samples, brightly colored regions were primarily concentrated in the outer regions of the specimens, whereas

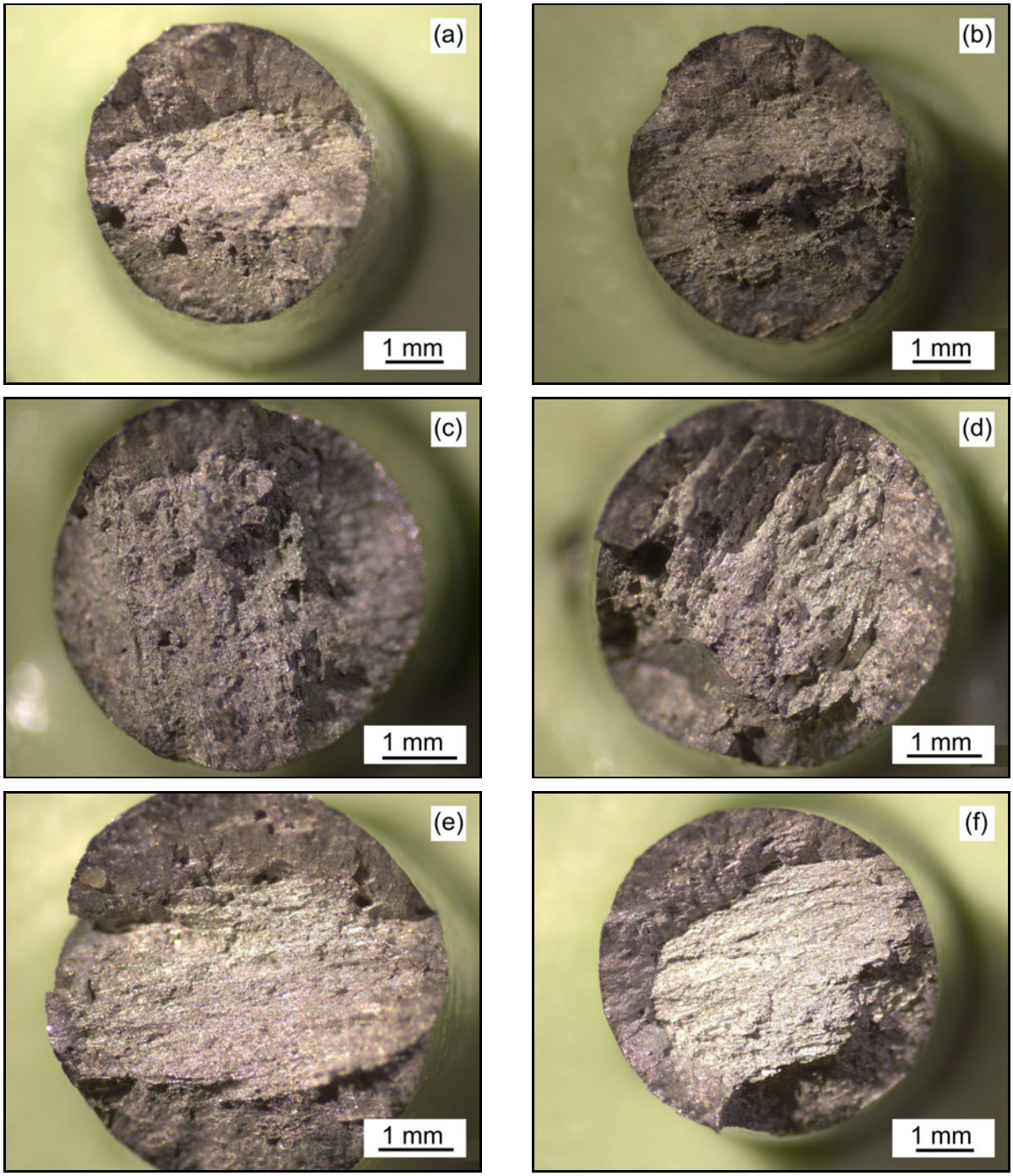

Fig. 15. Fracture surfaces of horizontally built samples: (a) HT1, (b) HT2, (c) HT3, (d) HT4, (e) HT5, and (f) HT6.

such regions were absent in the horizontally produced samples. These brightly colored regions varied in size and may be associated with defects that occurred during part production. Under tensile loading, such defects may have acted as stress concentrators, promoting localized brittle fracture. Consequently, bright-colored brittle fracture regions appeared along the outer portions of the fracture surfaces in the vertically built samples. In PBF-EB, the electron beam follows a raster scan pattern across the build platform, and pores tend to accumulate at the turning points at the sample edges [43]. S. Tammas-Williams et al. discovered that under standard build conditions, porosity measurements revealed two peaks as one moved inward from a section's edge. These peaks were both linked to the boundaries of the hatching region. The first peak was associated with gas bubbles being transported to the edge of each hatch pass and deposited when the melt pool changed direction. The second peak was associated with the beam's turning function

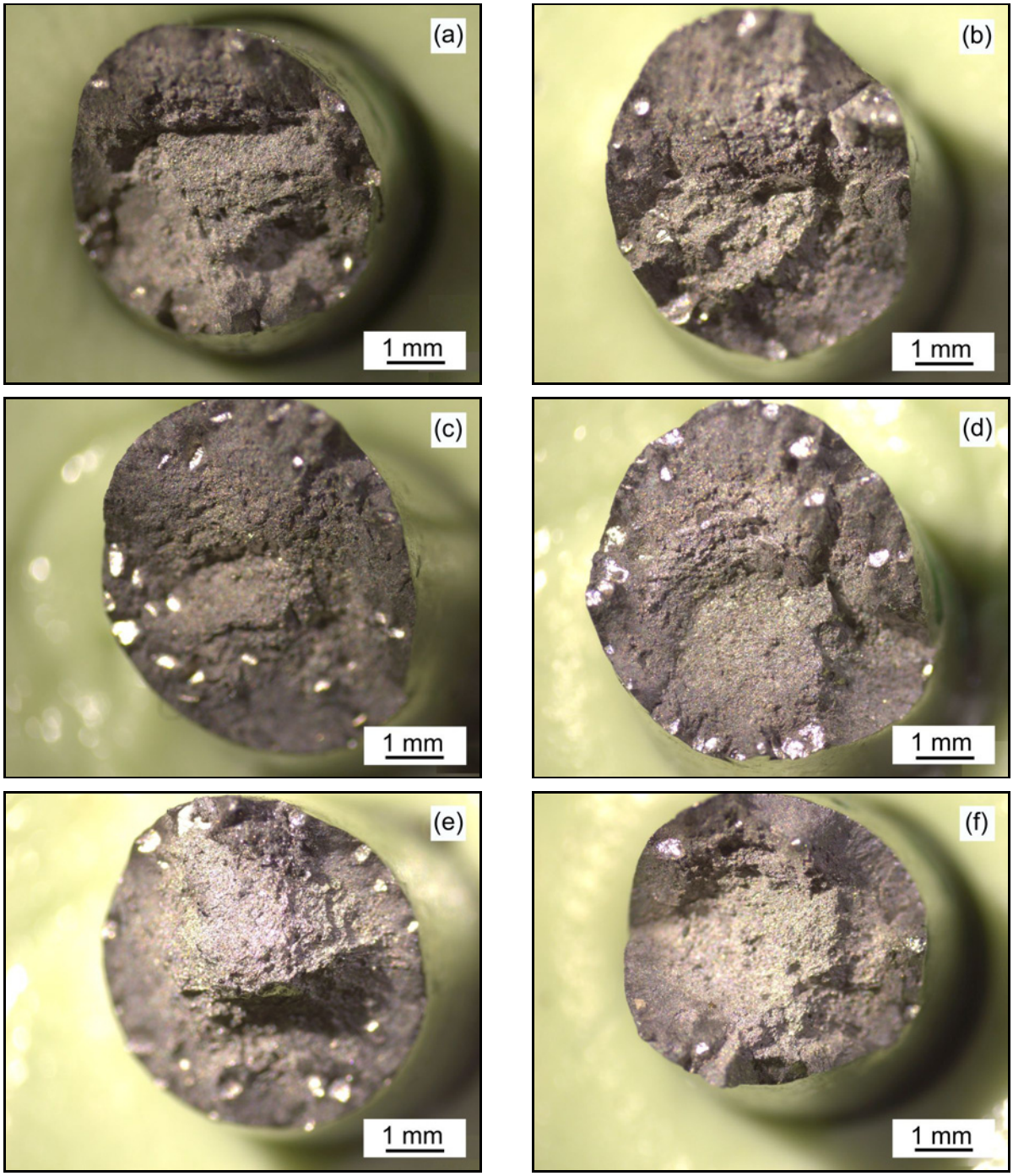

Fig. 16. Fracture surfaces of vertically built samples: (a) HT1, (b) HT2, (c) HT3, (d) HT4, (e) HT5, and (f) HT6.

within the hatching region, where overcompensation for residual heat led to an acceleration exceeding the beam's maximum during trajectory reversal. This resulted in insufficient energy density, thereby increasing gas pore formation near the edge of the hatched region [44]. Kirim et al. also demonstrated that the turning point function influences melt pool stability near part edges by increasing beam speed. They further emphasized that energy density decreases dramatically toward the end of a scan vector, significantly affecting heat transfer [45]. These defects, located in the outer regions of the specimens, can be linked to the reduced ductility observed in vertically built samples.

The HIP temperature modification influenced the microstructure, as discussed previously. Applying HIP at 800 ℃ (HIP1) led to the coarsening of α laths; however, this coarsening was limited (4 % for horizontal, 10 % for vertical) due to the low HIP temperature (Figs. 17, 18, and Table 3). Raising the HIP temperature to 920 ℃ led to more pronounced coarsening

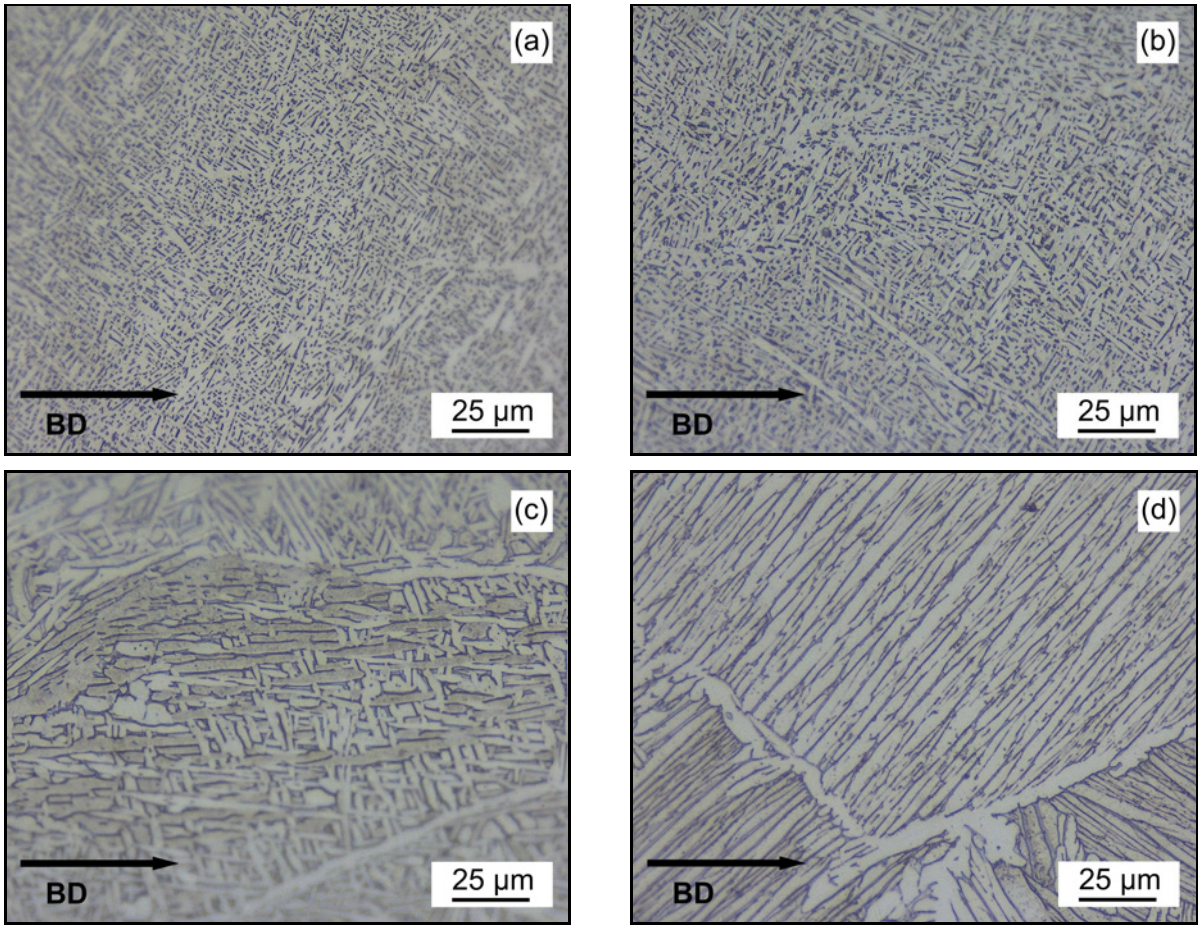

Fig. 17. OM images of the etched samples horizontally built: (a) as-built, (b) HIP at 800 °C, (c) HIP at 920 °C, and (d) HIP at 1050 °C.

of the α laths (61 % for horizontal, 67 % for vertical). Moreover, globular-shaped α grains appeared locally in the microstructure. In contrast, the Super Transus HIP process caused more distinctive changes. The primary β columns transformed into equiaxed β grains, and an α colony-dominated microstructure replaced the Widmanstätten structure. Subtransus heat treatments exert minimal influence on the microstructure, preserving the columnar morphology and maintaining the width of the β columns. Below the transus, the growth of the β phase is restricted by the presence of the α phase, and the remaining α_{GB} layer hinders the widening of the columns. Consequently, microstructural changes at subtransus temperatures primarily affect the width of the α lamellae. Above the transus, impediments to β grain growth are removed. Supertransus treatments result in the rapid growth of β grains, forming equiaxed structures. During slow furnace cooling at this temperature, the α phase selectively nucleates at the β grain boundaries, forming a continuous α_{GB} layer. Subsequent α plates nucleate from this layer and grow into the β grains as parallel plates, belonging to the same α colony and exhibiting the same Burgers relationship variant [28]. The α-lath sizes followed the same trend as in as-built and heat-treated samples. Vertically built samples possessed finer α-laths than their horizontally built counterparts, attributable to higher cooling rates. The effects of different HIP routines on the microstructure were summarized in the schematic drawing in Fig. 19.

The phase composition after HIPping, as determined by XRD, further elucidates the microstructural changes. The XRD results for the HIP-treated Ti-6Al-4V samples manufactured by PBF-EB (Fig. 20) reveal a clear dependence of detected α/β phase fractions on HIP temperature. At low-temperature HIPping (HIP1), both horizontally and vertically built samples exhibit a noticeable reduction in β-peak intensity. While this trend suggests partial decomposition or redistribution of the retained β phase, the attenuation may also be influenced by the partial overlap of β reflections with nearby α peaks and by orientation-dependent intensity suppression inherent to the textured PBF-EB microstructure. At moderate HIP temperatures (HIP2), both build orientations exhibit increased β-peak intensity. This enhancement indicates that the HIP2 temperature promotes stabilization or reprecipitation of the β phase, facilitated by increased

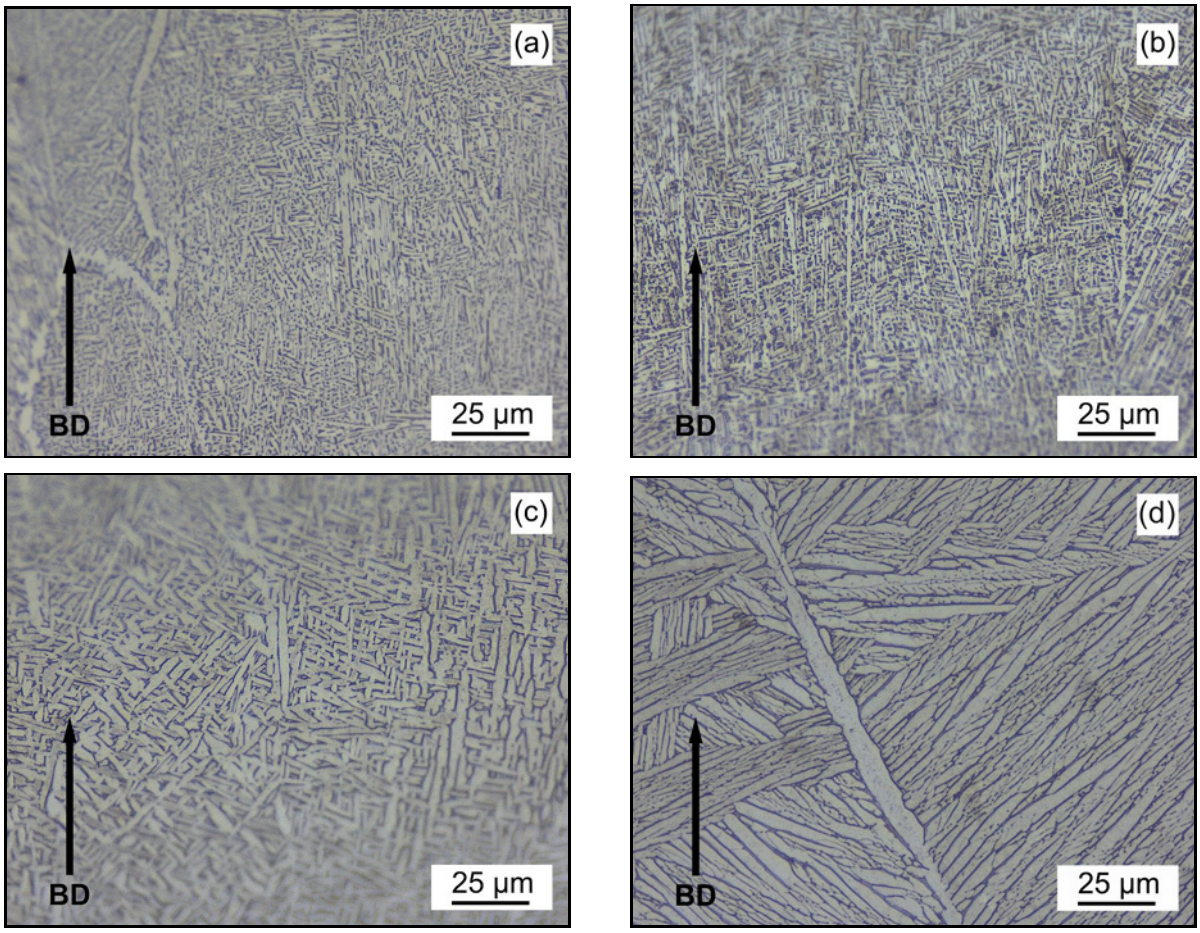

Fig. 18. OM images of the etched samples vertically built: (a) as-built, (b) HIP at 800 °C, (c) HIP at 920 °C, and (d) HIP at 1050 °C.

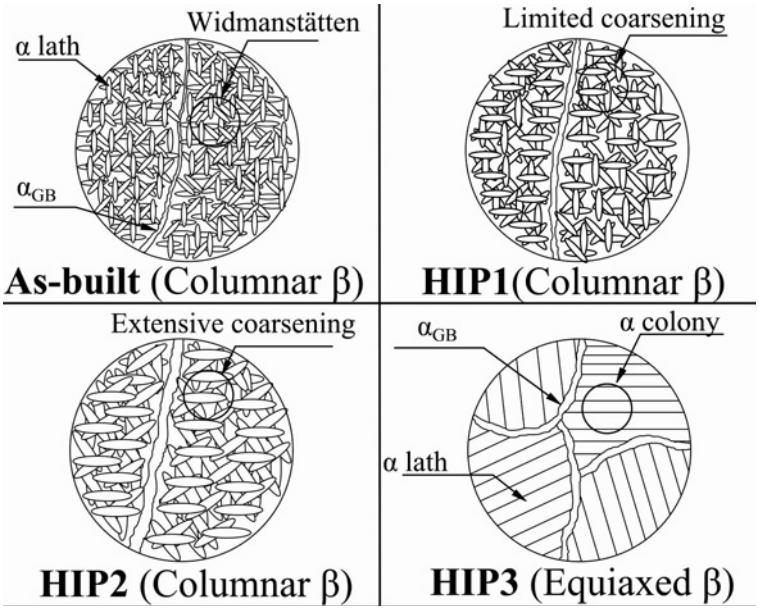

Fig. 19. Schematic illustration summarizing the effect of different HIP routines on the microstructure.

diffusion of β-stabilizing elements, such as V, during the HIP cycle. The appearance of stronger β reflections in both horizontal and vertical builds suggests that this temperature enables consistent β-phase evo-

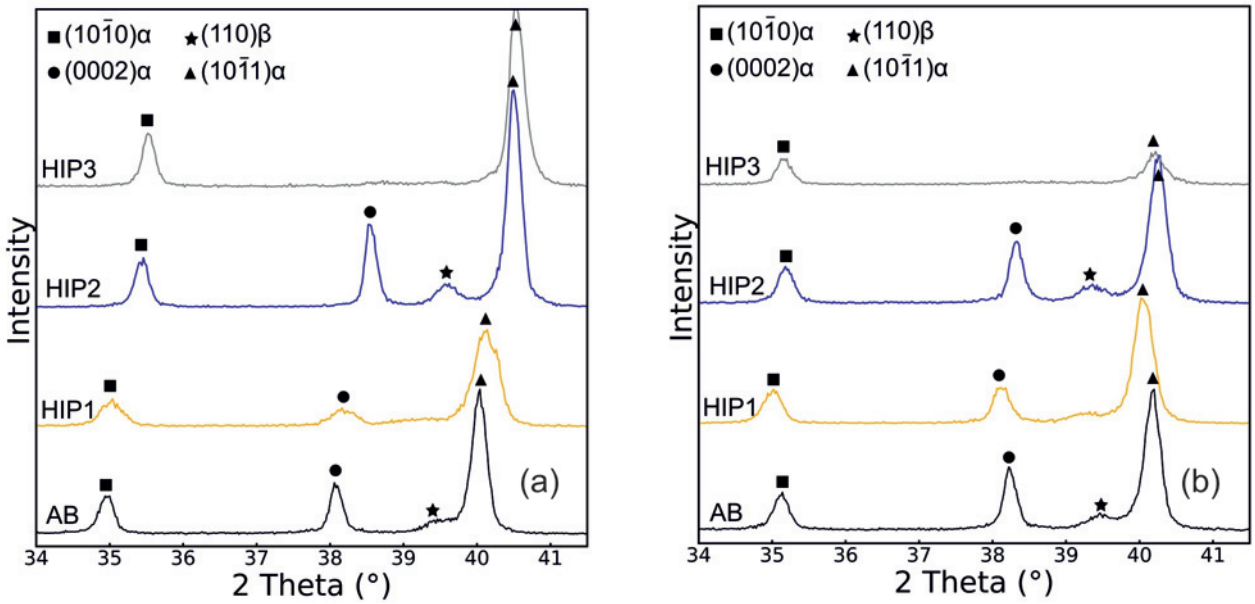

Fig. 20. XRD result of the HIPped samples: (a) horizontally as-built-HIP1-HIP2-HIP3, and (b) vertically as-built-HIP1-HIP2-HIP3.

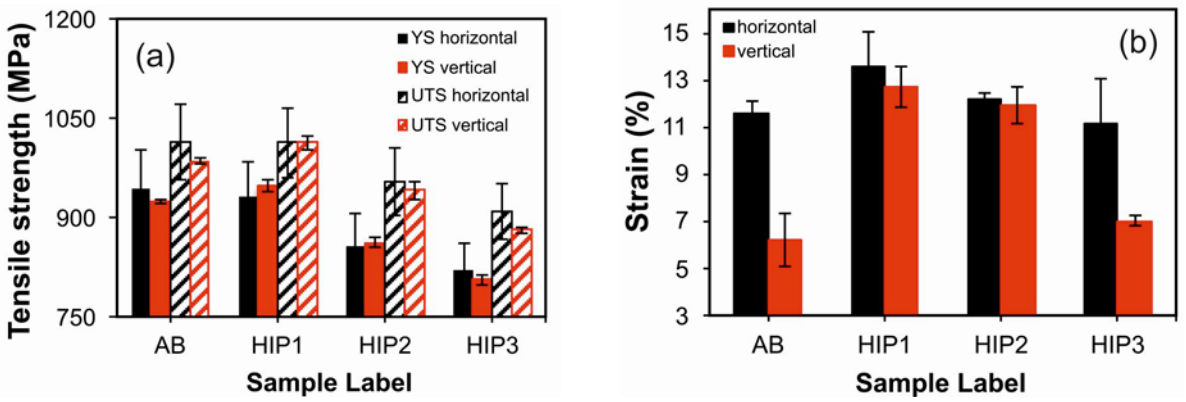

Fig. 21. Tensile test results of as-built and HIPped samples: (a) yield and ultimate tensile strength and (b) elongation to fracture.

lution regardless of the build direction, thereby mitigating texture differences typical of PBF-EB Ti-6Al-4V. When the HIP temperature is raised to super transus levels (HIP3), distinct β peaks are no longer detectable. However, this absence should not be interpreted as a complete elimination of the β phase. At temperatures above the β transus, Ti-6Al-4V transforms fully to the β field, and the resulting α/β morphology is determined by the cooling path after HIPping. The simultaneous disappearance of the (0002)α reflection in the HIP3 samples strongly indicates the formation of a pronounced α texture during post-transus cooling. Such texture effects, well known in PBF-EB Ti-6Al-4V, can significantly suppress specific α- and β-diffraction peaks, thereby limiting their detectability. Additionally, peak overlap complicates the identification of weak β reflections under these conditions. Overall, the HIP experiments demonstrate that the detectability of the β phase in PBF-EB Ti-6Al-4V is governed not only by temperature-driven phase transformations but also by the combined effects of peak overlap and the strong crystallographic textures inherent to additively manufactured microstructures, particularly following super-transus HIPping.

The mechanical performance of the HIP-processed samples reflects the combined effects of densification and microstructural evolution. Tensile results indicated that the HIP1 process did not cause a significant loss of strength in horizontally built samples, with only a 1.2 % reduction in YS (Fig. 21). Additionally, it increased the strength in vertically built samples (2.5 % in YS), despite the observed coarsening of α. The HIP1 process improved the elongation-to-fracture in both horizontally (17 %) and vertically (104 %) built samples, with a more pronounced improvement in the vertically built samples. The rela-

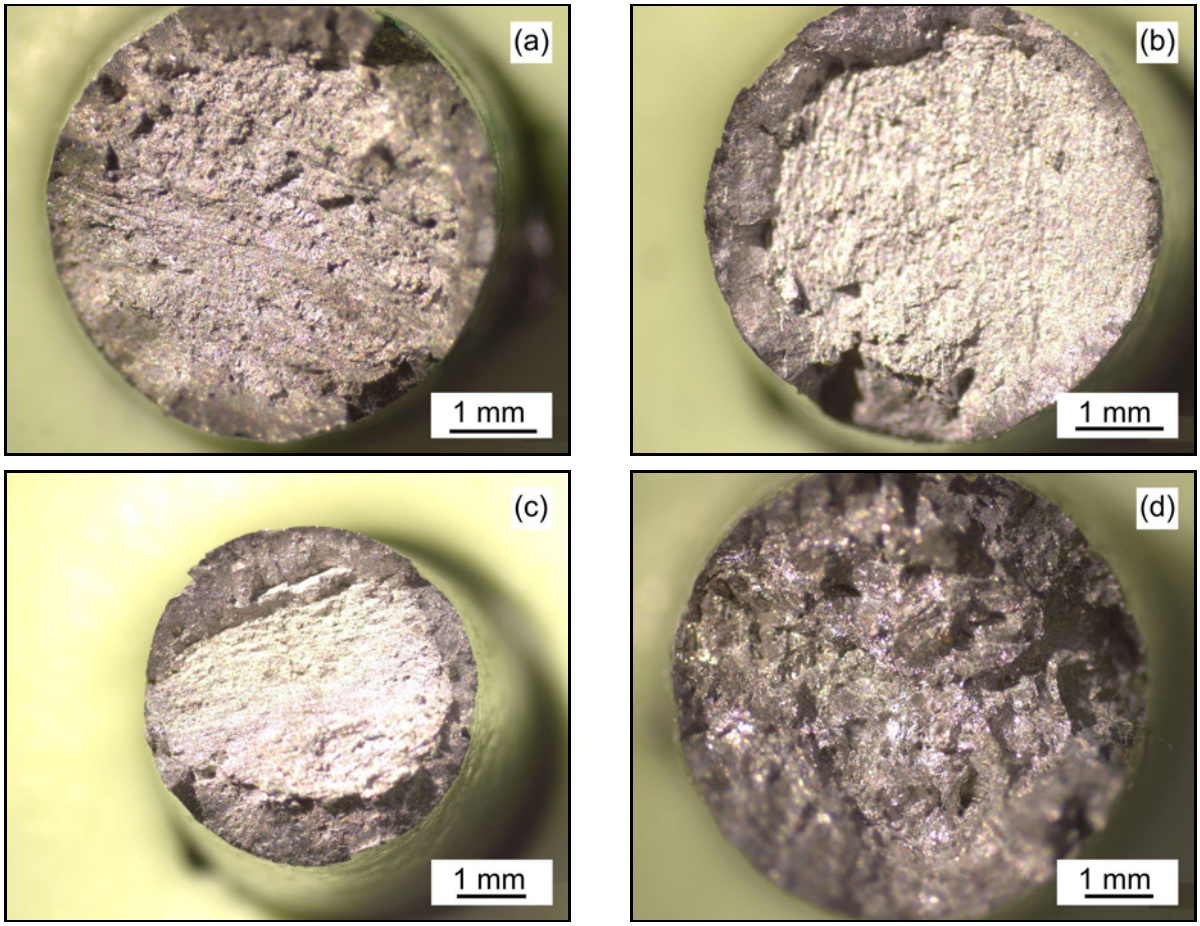

Fig. 22. Fracture surfaces of horizontally built samples: (a) as-built, (b) HIP1, (c) HIP2, and (d) HIP3.

tively low temperature and high pressure of the HIP1 treatment facilitated densification, resulting in a finer microstructure and lower β-phase content. Increasing the HIP temperature to 920 ℃ (HIP2) also resulted in higher ductility. However, a noticeable loss of strength was observed, with the yield strength decreasing by approximately 9 % in the horizontal samples and 6 % in the vertical samples. This decrease in strength can be attributed to the higher β-phase content and the thickening of the α phase. Samples processed through a super-transus HIP cycle performed the lowest mechanical strength and ductility, with high anisotropy. Compared with the as-built condition, HIP3 samples exhibited 12 % lower yield strength and 10 % lower ultimate tensile strength in both build orientations. Furthermore, the HIP3 process reduced ductility by 3.7 % in the horizontally built samples. The transformation of the microstructure from basketweave to colony-dominated may have altered the deformation behavior, and the coarser α lath thickness could have contributed to the reduced strength of the samples. The strong α texture may have led to anisotropy in the mechanical behavior of these specimens.

Finally, the fracture surfaces of HIP-treated samples corroborate the tensile data. The effects of the HIP processes on the fracture surfaces of vertically and horizontally built samples are shown in Figs. 22 and 23, respectively. After the HIP1 process, both vertically and horizontally built samples displayed a more evident cup-and-cone failure mode, with more pronounced shear lips. Findings indicate a more ductile fracture, which is consistent with the tensile test results. Furthermore, defects in the outer region of the vertically as-built samples were not observed in samples treated by the HIP1 process, suggesting that the HIP process closes defects. Samples processed with HIP2 also showed cup-and-cone fracture features, characterized by an inner flat fibrous region and outer shear lips. In contrast, the samples treated with the supertransus HIP (HIP3) process did not show the same trend. Draleos et al. showed strain concentrations in the selectively oriented α colonies of samples treated with supertransus-temperature HIP. Strain concentration results in widespread cracking along colony boundaries during tensile tests [33]. Localized deformation may explain the lower ductility observed in samples subjected to HIP at supertransus temperatures compared to those treated at subtransus temperatures. Magnified fracture images of samples treated with HIP at supertransus temperatures show similar

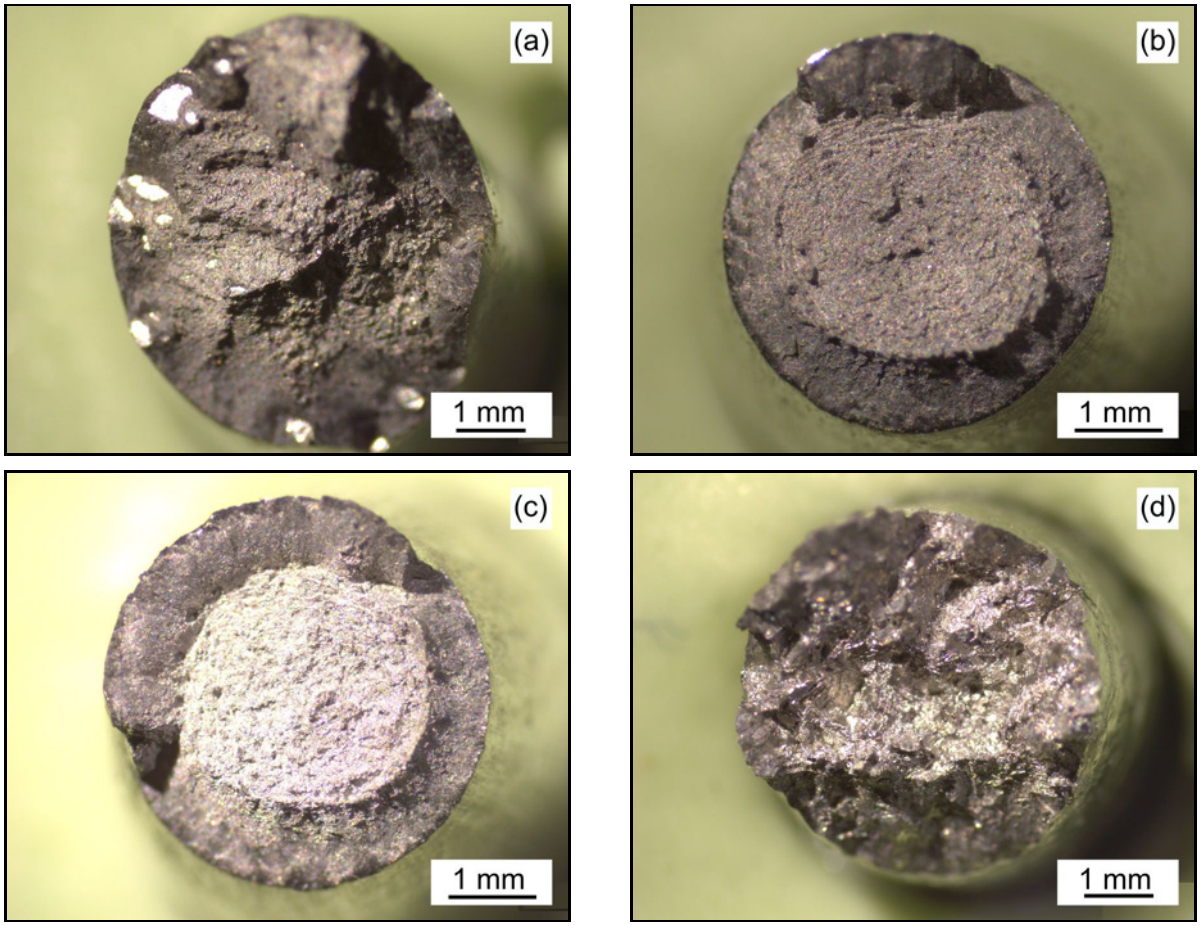

Fig. 23. Fracture surfaces of vertically built samples: (a) as-built, (b) HIP1, (c) HIP2, and (d) HIP3.

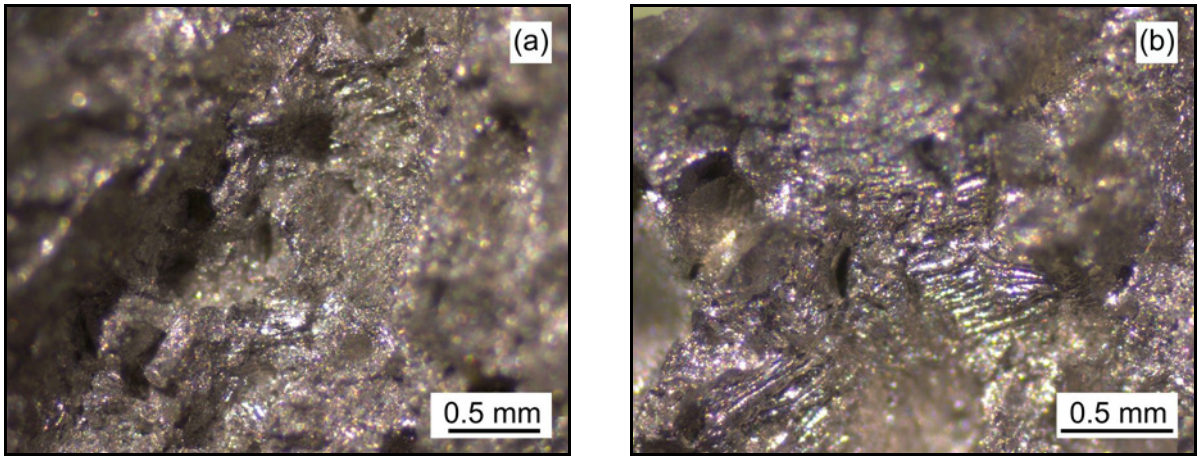

Fig. 24. Fracture surfaces of HIP3 samples: (a) horizontally and (b) vertically built.

features to those reported by Draleos et al. (Fig. 24). Fracturing along the boundaries of clusters of α-phase lamellae, leading to a feather-like overall fracture morphology, is evident on the fracture surface. These characteristics are more pronounced in the vertically constructed samples, which demonstrate reduced ductility in tensile tests. This could be attributed to the pronounced α-phase texture.

4. Conclusions

The influence of post-thermal processes on the microstructure and mechanical properties of Ti-6Al-4V alloy produced by PBF-EB was investigated. The major findings of this study can be summarized as follows:

1. The presence of porosities in both horizontally and vertically built samples, with higher poros-

ity observed in the vertically produced samples, is attributed to higher cooling rates. Heat treatments did not significantly affect porosity, whereas HIP processes effectively improved density.

2. As-built microstructure consisted of typical columnar primary β grains aligned parallel to build direction and an internal Widmanstätten $\alpha + \beta$ structure. In heat-treated samples, the microstructure identical to PBF-EB is also preserved. Solution treatment reduced the yield and tensile strength by $\sim 13\,\%$ and $\sim 6\,\%$, respectively. However, subsequent aging restored it by increasing α-phase content.

3. Sub-transus HIP processes maintained columnar primary β grains, super-transus HIP converted β grains to equiaxed morphology.

4. Low-temperature HIP with high pressure (HIP1) provided the most balanced performance. HIP1 improved ductility by 17 % in horizontal parts, with a minimal 1 % strength loss. In the vertical parts, it simultaneously increased ductility by 104 % and yield strength by 2.5 %. Its high pressure ensured effective pore closure and densification. At the same time, its low temperature limited α-lath coarsening, preserving a finer microstructure. Average α-lath size was increased from 1.69 to 1.77 µm for horizontally built samples and from 1.42 to 1.54 µm for vertically built samples after the HIP1 process. Conversely, a moderate HIP temperature (HIP2) led to a 9 % reduction in strength due to coarsening (the average α-lath size increased to 2.74 µm and 2.34 µm for horizontal and vertical samples, respectively).

5. The supertransus HIP (HIP3) cycle produced the lowest strength (12 % reduction for both alignment) and reduced ductility, resulting from its dramatically coarsened microstructure and altered deformation mechanisms. This condition also resulted in the most anisotropic ductility among the HIP cycles, attributable to its colony-dominated microstructure and strong α texture.

References

[1] M. Karasoglu, E. Yasa, E. Tan, A. Yagmur, Comparative and Experimental Study on the Effect of Heat Treatment Cycles for PBF Ti6Al4V, Proceedings of the 32nd Annual International Solid Freeform Fabrication Symposium – An Additive Manufacturing Conference, SFF (2021), pp. 1076–1092.

[2] C. Körner, Additive manufacturing of metallic components by selective electron beam melting — a review, Int. Mater. Rev. 61 (2016) 361–377. https://doi.org/10.1080/09506608.2016.1176289

[3] L. Zhang, Y. Liu, S. Li, Y. Hao, Additive manufacturing of titanium alloys by electron beam melting: A review, Adv. Eng. Mater. 20 (2018) 1700842. https://doi.org/10.1002/adem.201700842

[4] S. Liu, Y. C. Shin, Additive manufacturing of Ti6Al4V alloy: A review, Mater. Des. 164 (2019) 107552. https://doi.org/10.1016/j.matdes.2018.107552

[5] Ó. Teixeira, F. J. G. Silva, L.P. Ferreira, E. Atzeni, A review of heat treatments on improving the quality and residual stresses of the Ti–6Al–4V parts produced by additive manufacturing, Metals 10 (2020) 1006. https://doi.org/10.3390/met10081006

[6] H. D. Nguyen, A. Pramanik, A. K. Basak, Y. Dong, C. Prakash, S. Debnath, S. Shankar, I. S. Jawahir, S. Dixit, D. Buddhi, A critical review on additive manufacturing of Ti-6Al-4V alloy: microstructure and mechanical properties, J. Mater. Res. Technol. 18 (2022) 4641–4661. https://doi.org/10.1016/j.jmrt.2022.04.055

[7] G. Del Guercio, M. Galati, A. Saboori, P. Fino, L. Iuliano, Microstructure and mechanical performance of Ti–6Al–4V lattice structures manufactured via electron beam melting (EBM): A review, Acta Metall. Sin. (Engl. Lett.). 33 (2020) 183–203. https://doi.org/10.1007/s40195-020-00998-1

[8] S. S. Al-Bermani, M. L. Blackmore, W. Zhang, I. Todd, The origin of microstructural diversity, texture, and mechanical properties in electron beam melted Ti-6Al-4V, Metall. Mater. Trans. A 41 (2010) 3422–3434. https://doi.org/10.1007/s11661-010-0397-x

[9] H. Galarraga, R. J. Warren, D. A. Lados, R. R. Dehoff, M. M. Kirka, P. Nandwana, Effects of heat treatments on microstructure and properties of Ti-6Al-4V ELI alloy fabricated by electron beam melting (EBM), Mater. Sci. Eng. A 685 (2017) 417–428. https://doi.org/10.1016/j.msea.2017.01.019

[10] R. Cunningham, A. Nicolas, J. Madsen, E. Fodran, E. Anagnostou, M. D. Sangid, A. D. Rollett, Analyzing the effects of powder and post-processing on porosity and properties of electron beam melted Ti-6Al-4V, Mater. Res. Lett. 5 (2017) 516–525. https://doi.org/10.1080/21663831.2017.1340911

[11] V. Chastand, P. Quaegebeur, W. Maia, E. Charkaluk. Comparative study of fatigue properties of Ti-6Al-4V specimens built by electron beam melting (EBM) and selective laser melting (SLM), Mater. Charact. 143 (2018) 76–81. https://doi.org/10.1016/j.matchar.2018.03.028

[12] N. Hrabe, R. White, E. Lucon, Effects of internal porosity and crystallographic texture on Charpy absorbed energy of electron beam melting titanium alloy (Ti-6Al-4V), Mater. Sci. Eng. A 742 (2019) 269–277. https://doi.org/10.1016/j.msea.2018.11.005

[13] S. L. Lu, H. P. Tang, S. M. L. Nai, J. Wei, M. Qian, Intensified texture in selective electron beam melted Ti-6Al-4V thin plates by hot isostatic pressing and its fundamental influence on tensile fracture and properties, Mater. Charact. 152 (2019) 162–168. https://doi.org/10.1016/j.matchar.2019.04.019

[14] S. Franchitti, C. Pirozzi, R. Borrelli, Influence of hot isostatic pressing and surface finish on the mechanical behaviour of Ti6Al4V processed by electron beam melting, Fatigue Fract. Eng. Mater. Struct. 43 (2020) 2828–2841. https://doi.org/10.1111/ffe.13295

[15] L. Facchini, E. Magalini, P. Robotti, A. Molinari, Microstructure and mechanical properties of Ti-6Al-4V produced by electron beam melting of pre-alloyed powders, Rapid Prototyp. J. 15 (2009) 171-178. https://doi.org/10.1108/13552540910960262

[16] P. Nandwana, Y. Lee, C. Ranger, A. D. Rollett, R. R. Dehoff, S. S. Babu, Post-processing to modify the α phase micro-texture and β phase grain morphology

in Ti-6Al-4V fabricated by powder bed electron beam melting, Metall. Mater. Trans. A 50 (2019) 3429–3439. https://doi.org/10.1007/s11661-019-05247-4
[17] S. Raghavan, M. L. S. Nai, P. Wang, W. J. Sin, T. Li, J. Wei, Heat treatment of electron beam melted (EBM) Ti-6Al-4V: Microstructure to mechanical property correlations, Rapid Prototyp. J. 24 (2018) 774–783. https://doi.org/10.1108/RPJ-05-2016-0070
[18] A. K. Syed, M. Awd, F. Walther, X. Zhang, Microstructure and mechanical properties of as-built and heat-treated electron beam melted Ti–6Al–4V, Mater. Sci. Technol. 35 (2019) 653–660. https://doi.org/10.1080/02670836.2019.1580434
[19] H. Galarraga, D. A. Lados, R. R. Dehoff, M. M. Kirka, P. Nandwana, Effects of the microstructure and porosity on properties of Ti-6Al-4V ELI alloy fabricated by electron beam melting (EBM), Addit. Manuf. 10 (2016) 47–57. https://doi.org/10.1016/j.addma.2016.02.003
[20] M. J. Donachie. Titanium: A Technical Guide, ASM International, 2000.
[21] Y. Zhai, H. Galarraga, D. A. Lados, Microstructure evolution, tensile properties, and fatigue damage mechanisms in Ti-6Al-4V alloys fabricated by two additive manufacturing techniques, Procedia Eng. 114 (2015) 658–666. https://doi.org/10.1016/j.proeng.2015.08.007
[22] A. Carrozza, G. Marchese, A. Saboori, E. Bassini, A. Aversa, F. Bondioli, D. Ugues, S. Biamino, P. Fino, Effect of aging and cooling path on the super β-transus heat-treated Ti-6Al-4V alloy produced via Electron Beam Melting (EBM), Materials 15 (2022) 4067. https://doi.org/10.3390/ma15124067
[23] G. Soundarapandiyan, R. Khan, C. Johnston, B. Chen, M. Fitzpatrick, Effect of postprocessing thermal treatments on electron-beam powder bed–fused Ti6Al4V, Mater. Des. Process. Commun. 3 (2021) e168. https://doi.org/10.1002/mdp2.168
[24] ASTM B822-20, Standard Test Method for Particle Size Distribution of Metal Powders and Related Compounds by Light Scattering. ASTM International, West Conshohocken, 2025.
[25] ASTM B213-20, Standard Test Methods for Flow Rate of Metal Powders Using the Hall Flowmeter Funnel. ASTM International, West Conshohocken, 2025.
[26] ASTM E8/E8M-13a, Standard Test Methods for Tension Testing of Metallic Materials. ASTM International, West Conshohocken, 2013.
[27] K. Puebla, L. E. Murr, S. M. Gaytan, E. Martinez, F. Medina, R. B. Wicker, Effect of melt scan rate on microstructure and macrostructure for electron beam melting of Ti-6Al-4V, Mater. Sci. Appl. 3 (2012) 259–264. https://doi.org/10.4236/msa.2012.35038
[28] C. de Formanoir, S. Michotte, O. Rigo, L. Germain, S. Godet, Electron beam melted Ti–6Al–4V: Microstructure, texture and mechanical behavior of the as-built and heat-treated material, Mater. Sci. Eng. A 652 (2016) 105–119. https://doi.org/10.1016/j.msea.2015.11.052
[29] A. Gupta, C. J. Bennett, W. Sun, The role of defects and characterisation of tensile behaviour of EBM Additive manufactured Ti-6Al-4V: An experimental study at elevated temperature, Eng. Fail. Anal. 120 (2021) 105115. https://doi.org/10.1016/j.engfailanal.2020.105115
[30] W. Radlof, C. Benz, H. Heyer, M. Sander, Monotonic and fatigue behavior of EBM manufactured Ti-6Al-4V solid samples: Experimental, analytical and numerical investigations, Materials 13 (2020) 4642. https://doi.org/10.3390/ma13204642
[31] N. Hrabe, T. Quinn, Effects of processing on microstructure and mechanical properties of a titanium alloy (Ti–6Al–4V) fabricated using electron beam melting (EBM), Part 2: Energy input, orientation, and location, Mater. Sci. Eng. A 573 (2013) 271–277. https://doi.org/10.1016/j.msea.2013.02.065
[32] X. Shui, K. Yamanaka, M. Mori, Y. Nagata, K. Kurita, A. Chiba, Effects of post-processing on cyclic fatigue response of a titanium alloy additively manufactured by electron beam melting, Mater. Sci. Eng. A 680 (2017) 239–248. https://doi.org/10.1016/j.msea.2016.10.059
[33] L. Draelos, P. Nandwana, A. Srivastava, Implications of post-processing induced microstructural changes on the deformation and fracture response of additively manufactured Ti–6Al–4V, Mater. Sci. Eng. A 795 (2020) 139986. https://doi.org/10.1016/j.msea.2020.139986
[34] C. Dharmendra, A. Hadadzadeh, B. S. Amirkhiz, A. Llyod, M. Mohammadi. Deformation mechanisms and fracture of electron-beam-melted Ti–6Al–4V, Mater. Sci. Eng. A 771 (2020) 138652. https://doi.org/10.1016/j.msea.2019.138652
[35] R. Alaghmandfard, D. Chalasani, A. Hadadzadeh, B. S. Amirkhiz, A. Odeshi, M. Mohammadi, Dynamic compressive response of electron beam melted Ti–6Al–4V under elevated strain rates: Microstructure and constitutive models, Addit. Manuf. 35 (2020) 101347. https://doi.org/10.1016/j.addma.2020.101347
[36] N. E. Paton, C. H. Hamilton, Microstructural influences on superplasticity in Ti-6AI-4V, Metall. Trans. A 10 (1979) 241–250. https://doi.org/10.1007/BF02817634
[37] S. S. Youssef, X. Zheng, S. Huang, Y. Ma, M. Qi, S. Zheng, J. Lei, R. Yang, Precipitation behavior of $\alpha 2$ phase and its influence on mechanical properties of binary Ti-8Al alloy, J. Alloys Compd. 871 (2021) 159577. https://doi.org/10.1016/j.jallcom.2021.159577
[38] S. Cao, C. V. S. Lim, B. Hinton, X. Wu, Effects of microtexture and Ti3Al ($\alpha 2$) precipitates on stress-corrosion cracking properties of a Ti-8Al-1Mo-1V alloy, Corros. Sci. 116 (2017) 22–33. https://doi.org/10.1016/j.corsci.2016.12.012
[39] L. Yao, Y. He, Z. Wang, B. Peng, G. Li, Y. Liu, Effect of heat treatment on the wear properties of selective laser melted Ti–6Al–4V alloy under different loads, Acta Metall. Sin. (Engl. Lett.) 35 (2022) 517–525. https://doi.org/10.1007/s40195-021-01280-8
[40] J. Su, H. Xie, C. Tan, Z. Xu, J. Liu, F. Jiang, J. Tang, D. Fu, H. Zhang, J. Teng, Microstructural characteristics and tribological behavior of an additively manufactured Ti-6Al-4V alloy under direct aging and solution-aging treatments, Tribol. Int. 175 (2022) 107763. https://doi.org/10.1016/j.triboint.2022.107763
[41] V. M. Kaoushik, U. Nichul, V. Chavan, V. Hiwarkar, Development of microstructure and high hardness of Ti6Al4V alloy fabricated using laser beam

powder bed fusion: A novel sub-transus heat treatment approach, J. Alloys Compd. 937 (2023) 168387. https://doi.org/10.1016/j.jallcom.2022.168387

[42] Y. Cao, M. Delin, F. Kullenberg, L. Nyborg, Surface modification of Ti-6Al-4V powder during recycling in EBM process, Surf. Interface Anal. 52 (2020) 1066–1070. https://doi.org/10.1002/sia.6847

[43] X. Zhao, S. Li, M. Zhang, Y. Liu, T. B. Sercombe, S. Wang, Y. Hao, R. Yang, L. E. Murr, Comparison of the microstructures and mechanical properties of Ti–6Al–4V fabricated by selective laser melting and electron beam melting, Mater. Des. 95 (2016) 21–31. https://doi.org/10.1016/j.matdes.2015.12.135

[44] S. Tammas-Williams, H. Zhao, F. Léonard, F. Derguti, I. Todd, P. B. Prangnell, XCT analysis of the influence of melt strategies on defect population in Ti–6Al–4V components manufactured by Selective Electron Beam Melting, Mater. Charact. 102 (2015) 47–61. https://doi.org/10.1016/j.matchar.2015.02.008

[45] B. Kirim, E. Soylemez, E. Tan, E. Yasa, Understanding Process Parameters Strategy to Simulate the Thermal Models of Electron Beam Melting, Proceedings of the Advances in Additive Manufacturing with Powder Metallurgy, AMPM (2022), pp. 15–25.